Seasonality in Prediction Skill and Predictable Pattern of Tropical Indian Ocean SST

JIESHUN ZHU

Center for Ocean–Land–Atmosphere Studies, George Mason University, Fairfax, Virginia, and Climate Prediction Center, National Centers for Environmental Prediction/NOAA, College Park, and Innovim, Greenbelt, Maryland

BOHUA HUANG

Center for Ocean–Land–Atmosphere Studies, and Department of Atmospheric, Oceanic, and Earth Sciences, College of Science, George Mason University, Fairfax, Virginia

ARUN KUMAR

Climate Prediction Center, National Centers for Environmental Prediction/NOAA, College Park, Maryland

JAMES L. KINTER III

Center for Ocean–Land–Atmosphere Studies, and Department of Atmospheric, Oceanic, and Earth Sciences, College of Science, George Mason University, Fairfax, Virginia

(Manuscript received 20 January 2015, in final form 30 June 2015)

ABSTRACT

Seasonality of sea surface temperature (SST) predictions in the tropical Indian Ocean (TIO) was investigated using hindcasts (1982–2009) made with the NCEP Climate Forecast System version 2 (CFSv2). CFSv2 produced useful predictions of the TIO SST with lead times up to several months. A substantial component of this skill was attributable to signals other than the Indian Ocean dipole (IOD). The prediction skill of the IOD index, defined as the difference between the SST anomaly (SSTA) averaged over 10°S–0°, 90°–110°E and 10°S–10°N, 50°–70°E, had strong seasonality, with high scores in the boreal autumn. In spite of skill in predicting its two poles with longer leads, CFSv2 did not have skill significantly better than persistence in predicting IOD. This was partly because the seasonal nature of IOD intrinsically limits its predictability.

The seasonality of the predictable patterns of the TIO SST was further explored by applying the maximum signal-to-noise (MSN) empirical orthogonal function (EOF) method to the predicted SSTA in March and October, respectively. The most predictable pattern in spring was the TIO basin warming, which is closely associated with El Niño. The basin mode, including its associated atmospheric anomalies, can be predicted at least 9 months ahead, even though some biases were evident. On the other hand, the most predictable pattern in fall was characterized by the IOD mode. This mode and its associated atmospheric variations can be skillfully predicted only 1–2 seasons ahead. Statistically, the predictable IOD mode coexists with El Niño; however, the 1994 event in a non-ENSO year (at least not a canonical ENSO year) can also be predicted at least 3 months ahead by CFSv2.

1. Introduction

Dynamical prediction of seasonal atmospheric climate largely relies on the ability to predict slow variations of anomalous boundary forcing, including sea surface temperature (SST) and land surface conditions (e.g., Charney and Shukla 1981), even though there is recent evidence showing that coupling processes can produce additional predictable signals (e.g., Zhu and Shukla 2013). Through their atmospheric teleconnection, SST variability in the tropical Pacific associated with El Niño–Southern Oscillation (ENSO) is considered to be the primary source of seasonal climate predictability (e.g., Trenberth et al. 1998; Hoerling and Kumar 2002). The ability of current dynamical models

Corresponding author address: Dr. Jieshun Zhu, Climate Prediction Center, 5830 University Research Court, College Park, MD 20740.
E-mail: jieshun.zhu@noaa.gov

DOI: 10.1175/JCLI-D-15-0067.1

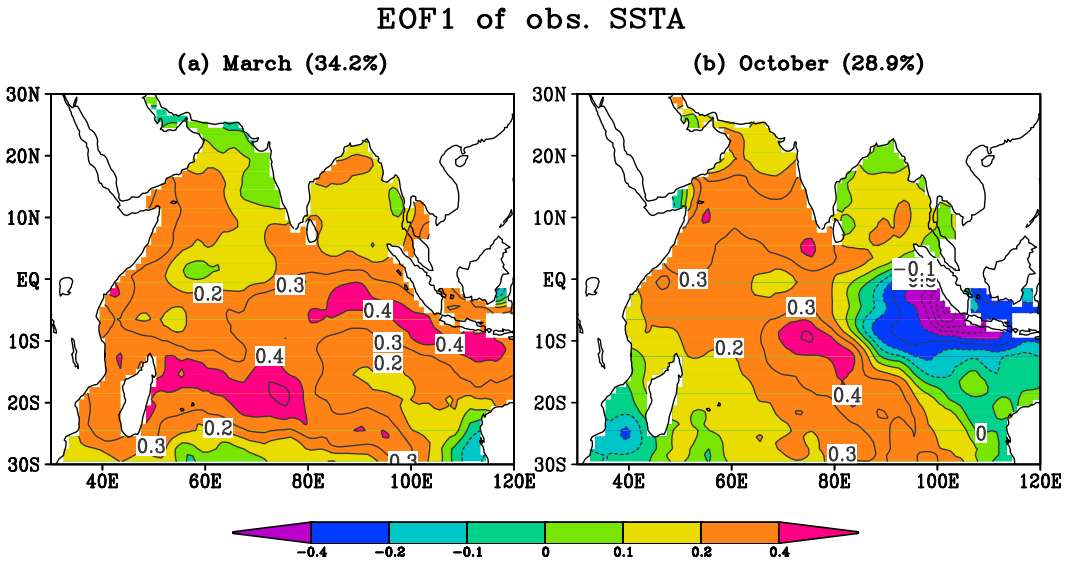

FIG. 1. The first EOF modes of observed SSTAs in (a) March (1983–2009) and (b) October (1982–2009). The explained percentages of the respective total variances are indicated in each panel. The contour interval is 0.1°C.

to predict ENSO has improved significantly since they were first used in this way about three decades ago (Cane et al. 1986). ENSO-related SST anomalies (SSTAs) in the tropical Pacific can now be successfully predicted several seasons ahead (e.g., Luo et al. 2005; Jin et al. 2008; Zhu et al. 2012b, 2013a,b, 2015; Xue et al. 2013).

In addition to tropical Pacific SSTAs, the SST in the other tropical basins can also stimulate weather and climate variability over the globe. For example, the precipitation over northeast Brazil (e.g., Hastenrath and Heller 1977) and sub-Saharan Africa (e.g., Lamb 1978) is associated with the meridional gradient of SST in the tropical Atlantic. Of greater relevance to this study, SST variations in the tropical Indian Ocean (TIO) are an important source of seasonal climate variability in the adjoining landmasses of eastern Africa (e.g., Clark et al. 2003), Asia (e.g., Guan and Yamagata 2003; Annamalai et al. 2005; Yang et al. 2007), and Australia (e.g., Nicholls 1989; Cai et al. 2011). Thus, predictions of SST evolution in the two tropical basins other than the Pacific are also of importance. In the case of the tropical Atlantic, however, current dynamical forecast systems are not skillful in predicting SST variations even compared with persistence (e.g., Stockdale et al. 2006; Hu and Huang 2007). The lack of prediction skill not only reflects the relatively lower predictability in the Atlantic, but is also due to model biases (e.g., Huang et al. 2007) and the quality of ocean initial conditions (e.g., Zhu et al. 2012a).

On the other hand, there are studies reporting some success in predicting low-frequency SST variations in the TIO, even though the skill is lower than that for ENSO. For example, Kug et al. (2004) developed a simple linear regression model with Niño-3 SST as the sole predictor, and yielded useful predictions of the basin-mean SST up to 6 months in advance. There are more studies of the prediction and predictability of the Indian Ocean dipole mode (IOD; e.g., Wajsowicz 2005, 2007; Luo et al. 2007, 2008; Song et al. 2008; Zhao and Hendon 2009; Shi et al. 2012). According to these studies, coupled systems generally have higher skill over the western pole of IOD than the eastern pole, with skillful predictions of SSTA reported at lead times of around 5–6 and 3–4 months, respectively. The lead time for skillful prediction of the IOD events themselves, even at their peak season (i.e., boreal autumn), is reported to be only about one season, although some strong individual IOD events are reported to be predictable at longer lead times (e.g., Luo et al. 2007, 2008; Shi et al. 2012). Moreover, some studies suggest that an IOD event may be more predictable if it occurs simultaneously with an El Niño (e.g., Song et al. 2008).

Most of the prediction and predictability studies discussed above are based on indices defined as SSTAs averaged in certain regions of the TIO, which, however, might not be adequate, especially when evaluating the prediction skill of the IOD index, given the potential effects of model bias. Furthermore, the strong seasonality of the TIO interannual variability should also be taken into account in evaluating the predictability of its major modes of variability. For instance, the pattern with opposite SSTA polarity in the eastern and western equatorial Indian Ocean (Fig. 1b) appears mainly in the boreal late summer and autumn. Therefore, one cannot

rule out the possibility that the IOD index might only be a statistical artifact (e.g., Baquero-Bernal et al. 2002) during the other seasons.

A basinwide warming or cooling (Fig. 1a) is more dominant in other seasons as another major TIO mode. As a response to ENSO, the TIO gradually warms up following an evolving El Niño event, reaching a maximum during spring (March–May) while expanding into the northwestern Pacific about one season after Niño-3 SST has peaked (Nigam and Shen 1993; Klein et al. 1999; Liu and Alexander 2007; Kumar et al. 2014). The formation of this basinwide warm pattern involves several potential mechanisms in response to ENSO. These include formation of a anticyclone over the Indian Ocean basin starting from the beginning of ENSO development (Klein et al. 1999; Lau and Nath 2003), the anomalous anticyclone near the Philippines that is remotely forced by the eastern equatorial Pacific SSTA in the ENSO mature phase (e.g., Wang et al. 2000; Jiang et al. 2013), and the thermocline deepening in the southwestern Indian Ocean during the same period (e.g., Huang and Kinter 2002; Xie et al. 2002; Huang and Shukla 2007a). These mechanisms provide the physical basis for the predictability for the basin wide warming at multiseasonal lead times. However, whether current seasonal forecast systems can reproduce these multiple processes synchronously to realize such potential predictability needs to be investigated. Therefore, it may be more useful to treat the whole TIO as a prediction objective.

In this study, in addition to examining the overall prediction skill similar to previous studies (Wajsowicz 2005, 2007; Luo et al. 2007, 2008; Song et al. 2008; Zhao and Hendon 2009; Shi et al. 2012), we also investigate the most predictable patterns by applying the maximum signal-to-noise (MSN) empirical orthogonal function (EOF) method to the predicted SSTA. Considering the seasonal features of both the basin warming mode and the IOD, the seasonal dependence of the predictable patterns is explored by applying the MSN EOF in different seasons. We examine whether current prediction systems [e.g., the Climate Forecast System, version 2 (CFSv2)] can capture the major modes of the TIO, and, if so, how well they can be predicted.

This paper is organized as follows. Section 2 briefly introduces the coupled climate prediction model (i.e., CFSv2), the hindcast datasets, and the analysis methods. Section 3 examines the overall prediction skill and the seasonal dependence of SSTAs on the TIO. Sections 4 and 5 respectively explore the most predictable modes in SSTAs during March and October by applying the MSN EOF method. The associations between these patterns and the conditions in the TIO and the tropical Pacific are also investigated. A summary and discussion is given in section 6.

2. Data and analysis methods

The retrospective 9-month hindcasts analyzed in this work are from the NCEP Climate Climate Forecast System Reanalysis and Reforecast (CFSRR) Project using CFSv2 (Saha et al. 2014), which includes predictions initialized in all calendar months from January 1982 to December 2009. The retrospective 9-month forecasts have initial conditions (ICs) at 0000, 0600, 1200, and 1800 UTC on every 5th day, starting from 0000 UTC 1 January of every year, with oceanic and atmospheric ICs from the NCEP Climate Forecast System Reanalysis (CFSR; Saha et al. 2010). There are 292 forecasts for every year.

In CFSv2, the ocean component model is the GFDL MOM version 4, which is configured for the global ocean with a horizontal grid of $0.5° \times 0.5°$ poleward of 30°S and 30°N and meridional resolution increasing gradually to 0.25° between 10°S and 10°N. The vertical coordinate is oceanic depth with 40 levels (27 in the upper 400 m). The maximum depth is approximately 4.5 km. The atmospheric component model is the NCEP Global Forecast System (GFS), which has horizontal resolution at T126 (105-km grid spacing spacing; reduced from the GFS resolution for operational numerical weather prediction) and 64 vertical levels in a hybrid sigma-pressure coordinate. The oceanic and atmospheric components exchange surface momentum, heat, and freshwater fluxes, as well as SST, every 30 min. CFSv2 became the NCEP operational forecast system for seasonal-to-interannual prediction in March 2011. It has been shown to have good prediction skill in the tropical Pacific (Zhu et al. 2012b, 2014; Xue et al. 2013) and reasonable skill in some extratropical oceans including the North Atlantic (Hu et al. 2013), the North Pacific (Hu et al. 2014), and the southern subtropical Pacific (Guan et al. 2014).

For this analysis, the ensemble mean predictions are comprised of 24 forecasts, whose ICs are from dates prior to the 7th of the "start month." As an example, for an ensemble monthly prediction with start month of September, the 24 ensemble members are the predictions from ICs on 9, 14, 19, 24, and 29 August and on 3 September, and each date has ICs at 0000, 0600, 1200, and 1800 UTC. Thus, by definition, the starting month (or lead month 0) of the prediction is an ensemble combination of predictions ranging over 25 days of ICs.

The prediction skill of CFSRR is first compared against persistence forecasts of the observed monthly mean SSTA. It should be pointed out that the definition of lead time is slightly different for persistence and CFSRR forecasts. Using September as an example of start month, for a persistence forecast, the September mean anomaly is assumed to remain unchanged through

the full forecast period, and the September (October) monthly mean is defined as a forecast at the zero- (one-) month lead. This implies a perfect skill at the zero-month lead for a persistence forecast. For CFSRR hindcast, however, because of the inherent feature of the ensemble generation method (i.e., lagged average), a September forecast (i.e., a forecast at the zero-month lead) is composed of forecasts beginning as early as 9 August. Therefore, a comparison based on the nominal lead time favors the persistence forecast, which includes more recent information from the observations. In addition, our analysis of forecast skill is based on monthly mean data, and thus our estimates of predictive skill are probably conservative in comparison with studies of skill assessment of 3- or 5-month means.

In this study, the conventional empirical orthogonal function (EOF) is used to derive the dominant modes of SSTA in March and October in observations. The most predictable patterns of SST are isolated by applying an EOF analysis with maximized signal-to-noise ratio (MSN EOF hereafter) to the predicted time series at given lead times. The MSN EOF is a method to derive patterns that optimize the signal-to-noise ratio from all ensemble members. It was developed by Allen and Smith (1997) and has been used widely, for example, by Venzke et al. (1999), Sutton et al. (2000), Chang et al. (2000), and Huang (2004) in extracting the dominant MSN EOF patterns in ensemble GCM integrations; by Hu and Huang (2007) in extracting the most predictable patterns of the tropical Atlantic in ensemble hindcasts; and by Zhu et al. (2012a) in extracting the common subsurface signals of the tropical Atlantic in multiple ocean analyses. The method assumes that in an ensemble of moderate size, the ensemble mean is supposedly composed of a signal and a nonnegligible random component. In general, the former may be attributable to the prescribed external boundary conditions or coupling processes (Zhu and Shukla 2013), while the later represents the unpredictable internal noise that is uncorrelated among ensemble members. Here, the signal represents the consistency among different members of the ensemble predictions because of the memory contained in the ICs. The leading MSN EOF mode is the one that maximizes ratio of the variance of the ensemble mean to the deviations among the ensemble members. In this work, we only analyze the leading MSN EOF mode, which is defined as the most predictable pattern. Details of this method are documented in Allen and Smith (1997), Venzke et al. (1999), and Huang (2004). In addition, a linear regression approach is also used to extract the patterns associated with a predefined time series or the time series associated with a specific spatial mode. It should be noted that, since the observations have only one realization and the CFSv2 predictions include 24 ensemble members, the observation-related regressions are expected to be weaker and less significant because of the lower noise level. Correlations are calculated to examine the consistency in time among different datasets.

The observation-based monthly SST analysis for validation is from the Optimum Interpolation SST, version 2 (OISSTv2; Reynolds et al. 2002), which has a resolution of $1.0° \times 1.0°$. Sea level pressure (SLP) and wind stress from NCEP–U.S. Department of Energy (DOE) Atmospheric Model Intercomparison Project phase 2 (AMIP-II) reanalysis are taken as observations (Kanamitsu et al. 2002). Monthly precipitation from the National Oceanic and Atmospheric Administration's (NOAA) Climate Prediction Center (CPC) Merged Analysis of Precipitation (CMAP) (Xie and Arkin 1997; available online at http://ingrid.ldgo.columbia.edu/) is used as a proxy for rainfall observations, which is on a $2.5° \times 2.5°$ grid.

3. SST predictive skill in the tropical Indian Ocean

In this section, we analyze the SSTA predictive skill in the tropical Indian Ocean during 1982–2009. The skill is measured by the anomaly correlation and root-mean-square error (RMSE) with respect to the OISSTv2 SSTA. The predictive skill is also compared with that based on the corresponding persistence forecast. As one of the foci in this study, the seasonality of predictive skill is investigated as well.

In terms of SST systematic biases in the tropical Indian Ocean (figures not shown here, but available from http://www.cpc.ncep.noaa.gov/products/people/mchen/CFSv2HCST/metrics/climBias.html), CFSRR produces a general basinwide cold bias with the bias larger in the western basin than in the eastern basin, but there is also a subtle warm bias in the eastern basin in hindcasts starting in boreal fall and winter. Such distributions result in a cold bias in the climatological IOD SST index for all hindcasts.

Figures 2 and 3 show the horizontal distributions of SSTA prediction skill in the tropical Indian Ocean at each lead month for the CFSRR and persistence predictions, respectively. As in other models (e.g., Luo et al. 2005), CFSv2 generally shows lower skill in the TIO than in the tropical Pacific Ocean, but higher skill than in the tropical Atlantic (figures not shown here; see Guan et al. 2014). As expected, the prediction skill of CFSRR decreases with increasing lead time in the TIO (Fig. 2). Within the basin, at each lead time the model exhibits the highest prediction skill in the southwestern TIO, where ocean dynamics is vital in determining the SSTA evolution, and ENSO plays an important role as a

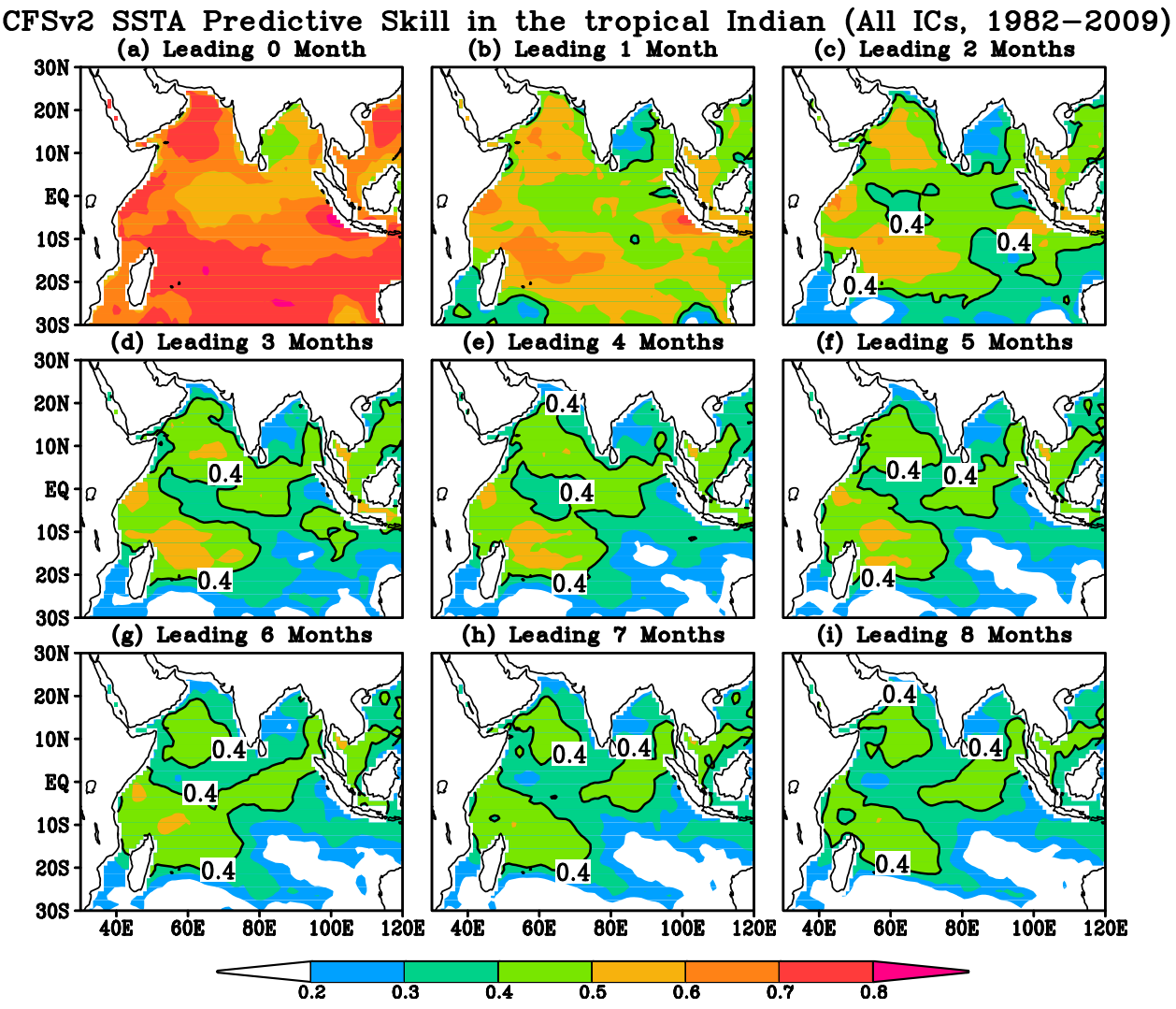

FIG. 2. Correlations between observed and CFSv2 predicted SSTAs in the tropical Indian at 0–8-month lead times, based on all ICs during January 1982–December 2009. The contour for 0.4 is highlighted.

remote forcing (Huang and Kinter 2002; Xie et al. 2002). In addition, the model also has some skill in the Arabian Sea and the region extending from the Andaman Sea to the central Indian Ocean. In these regions, the correlation skill can reach 0.4 at the 8-month lead time.

In comparison with the CFSRR prediction, the persistence prediction (Fig. 3) exhibits the highest skill in the equatorial Indian Ocean, where the correlation skill can be above 0.5 even at the 9-month lead time. It is noticeable that this long-persistence region is dynamically very active and is strongly influenced by the prevailing semiannual Wyrtki jet (Wyrtki 1973), as well as the ENSO-induced equatorial zonal wind anomalies. It is also possibly related to the multidecadal SST warming trend there (e.g., Luo et al. 2012). The skill in the same region, however, is much lower in CFSRR. More curiously, the CFSv2 prediction skill has a local minimum already at lead-month 0 (Fig. 2a) while a local maximum is maintained throughout all lead-months in persistence (Fig. 3). These differences imply that there are model deficiencies in representing related dynamical processes and unrealized potential predictability in current models. Except for this region, CFSRR generally has higher skill than persistence.

A more quantitative measure of the prediction skill of IOD, an important mode in the tropical Indian Ocean, is provided in Fig. 4, which shows the anomaly correlation and RMSE between the observed and predicted IOD indices and SSTA in its eastern and western poles (referred to as the EIO and WIO indices, respectively) as a function of lead month, based on all predictions during 1982–2009. As discussed in section 2, it should be noted

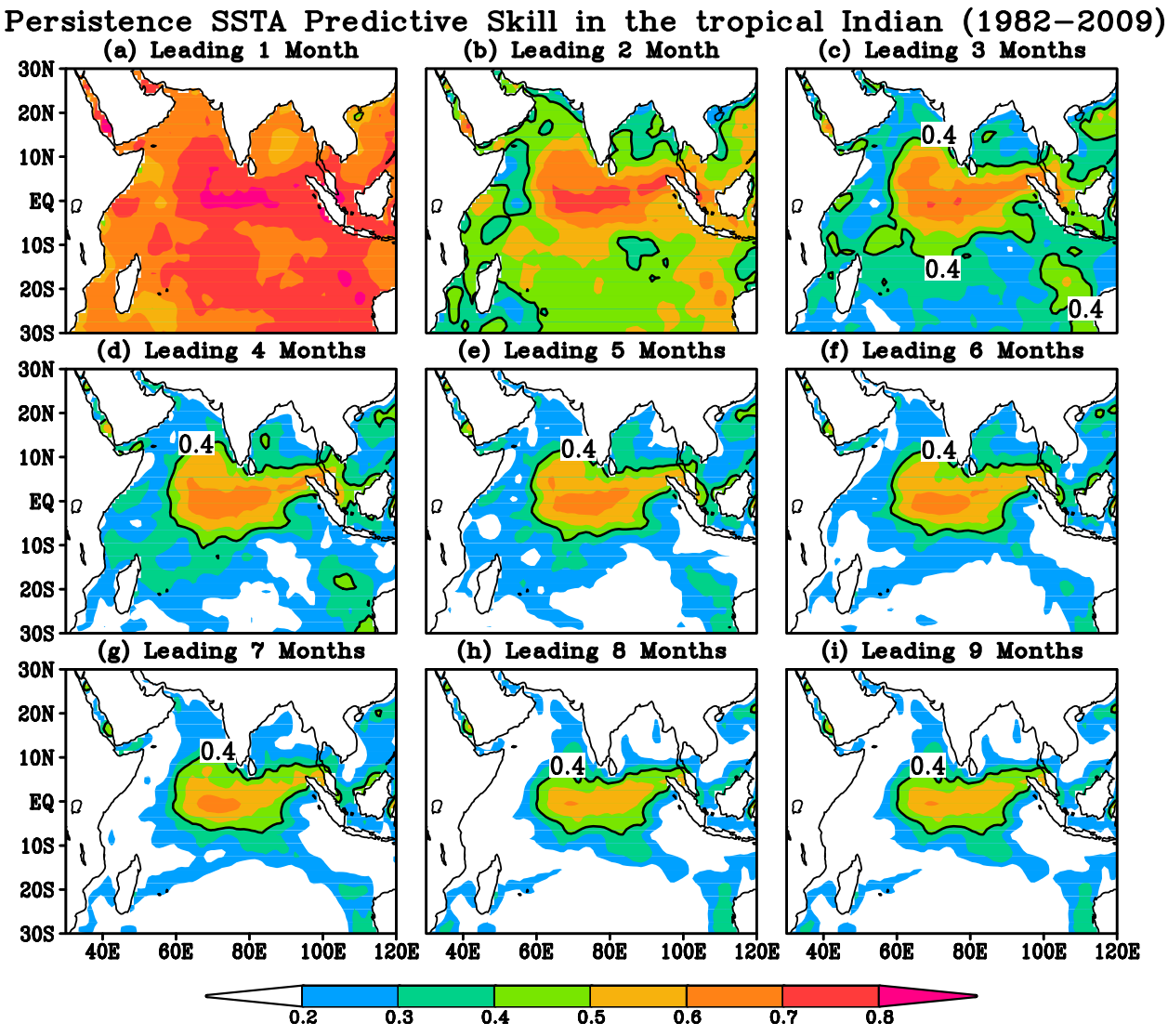

FIG. 3. Correlations between observed and persistence predicted SSTAs in the tropical Indian at 1–9-month lead times, based on all ICs during January 1982–December 2009. The contour for 0.4 is highlighted.

that the definition of lead time used herein favors the persistence forecast, which may give a misleading impression at short leads. For example, the persistence prediction at the 0-month lead, by definition, has perfect forecast skill (correlation 1 and RMSE 0), which always beats the CFSRR forecast at the 0-month lead. With the increase in lead times, the correlation (RMSE) generally drops (increases) for all three indices in both CFSRR and persistence forecasts. However, the prediction skill of persistence diminishes faster, and CFSRR quickly shows its supremacy at longer lead times. Taking the prediction of EIO as an example (Figs. 4c,d), the correlation (RMSE) skill in persistence drops (increases) rapidly from 1.0 (0.0°C) to less than 0.0 (~0.6°C) by the ninth lead month, while in CFSRR the correlation (RMSE) skill drops (increases) more slowly from ~0.87 (~0.30°C) to ~0.41 (~0.43°C). The WIO skill (Figs. 4a,b) is generally better than for EIO. In the CFSRR forecast, the correlation skill is well above 0.6 at 0–6-month lead times and only slightly below 0.6 at 7–9-month lead times. If a skillful prediction is defined as one having correlation higher than 0.6, CFSv2 can provide skillful predictions for the WIO index 2–3 seasons ahead, but for EIO only ~1 season can be achieved.

The better prediction skill in WIO than EIO is also evident in the RMSE measure and in the comparison to the persistence forecast as well. What is more interesting, even though the prediction skill of WIO and EIO looks useful, the IOD index itself (Figs. 4e,f) has much lower prediction skill, with skillful prediction

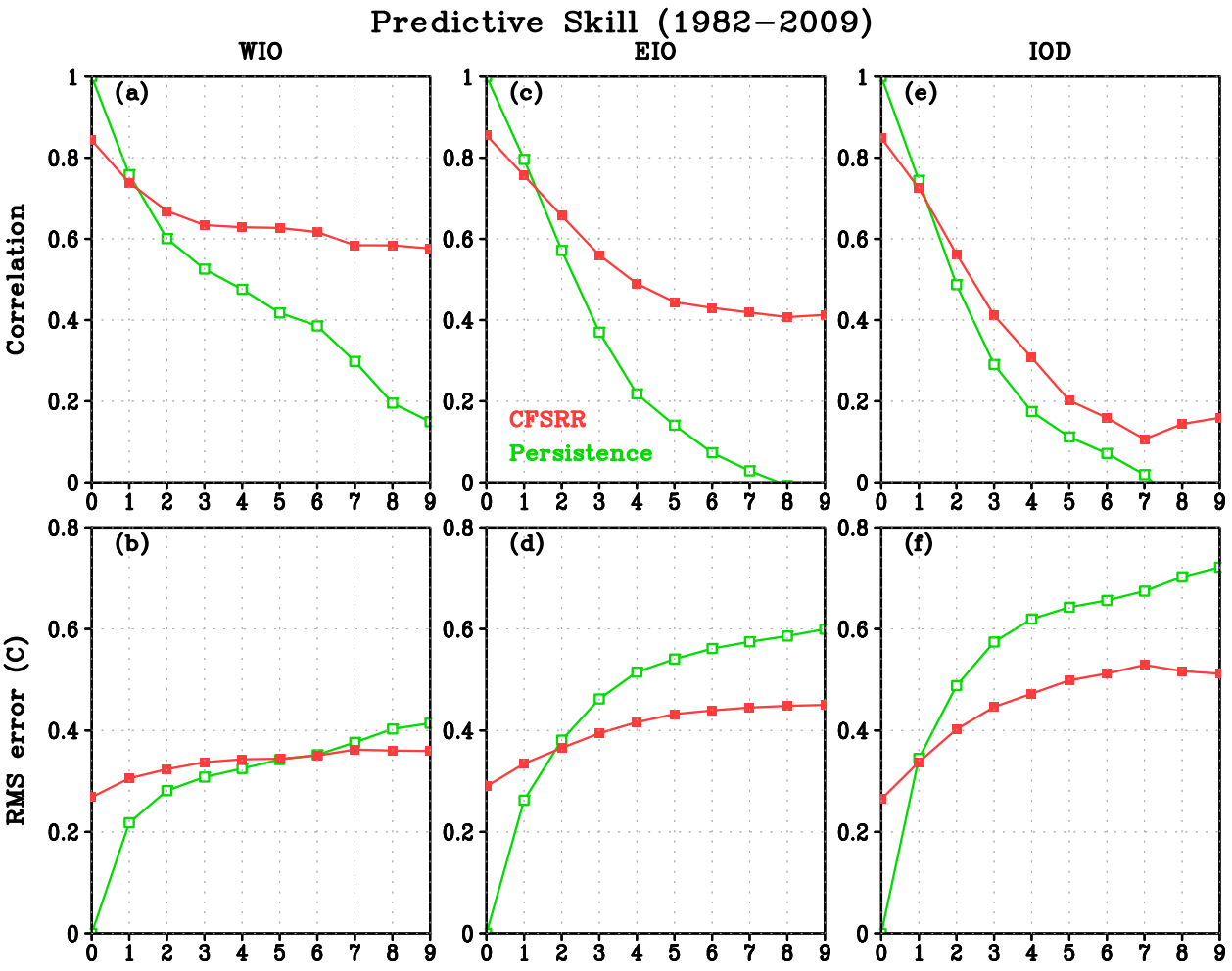

FIG. 4. (top) Anomaly correlation coefficients and (bottom) RMS errors (°C) of persistence (green lines) and CFSRR forecast (red lines) as a function of lead months for (a),(b) SST anomalies in the western pole of the Indian Ocean (WIO; 10°S–10°N, 50°–70°E), (c),(d) SST anomalies in the eastern pole of the Indian Ocean (EIO; 10°S–0°, 90°–110°E), and (e),(f) the IOD index, based on all predictions during 1982–2009.

available less than one season ahead. This paradox is a result of strong seasonality in the TIO variability. Specifically, IOD events take place during June–November, whereas the basin-scale warming following an El Niño event dominates during the rest of the year (Schott et al. 2009). As discussed below (Fig. 5), the relatively high skill for the WIO and EIO indices (Figs. 4a–d) is mainly related to the basin-scale warming mode, not the IOD mode.

Figure 5 explores the seasonality of the above prediction skill in both persistence and CFSRR forecasts, by showing the correlation skill of the three indices as functions of both IC month and lead time. A striking feature of Fig. 5 is that the prediction skill of the IOD index (Figs. 5e,f) strongly depends on season, both for persistence and CFSRR forecasts. Specifically, both forecasts generally show high prediction skill during the boreal autumn (especially the late autumn), but have low skill during other seasons, exhibiting a similar feature to the known boreal winter–spring predictability barrier (Wajsowicz 2005, 2007; Luo et al. 2007; Feng et al. 2014). Specifically, there are two prediction barriers: one is in December associated with the seasonal phase locking of IOD onto monsoonal winds; the other is in boreal spring associated with the influence of ENSO. As a result, the skillful predictions with the longest lead month are those initiated in summer (June–July) in both CFSRR and persistence forecasts. This feature is consistent with the seasonality attribute of IOD events, which develop in June and peak in October (Saji et al. 1999). It is interesting to note that the CFSRR apparently outperforms persistence in these long-lead predictions initiated in early summer.

For the WIO and EIO indices, the prediction skill in CFSRR (Figs. 5b,d) has a weak but discernible seasonality,

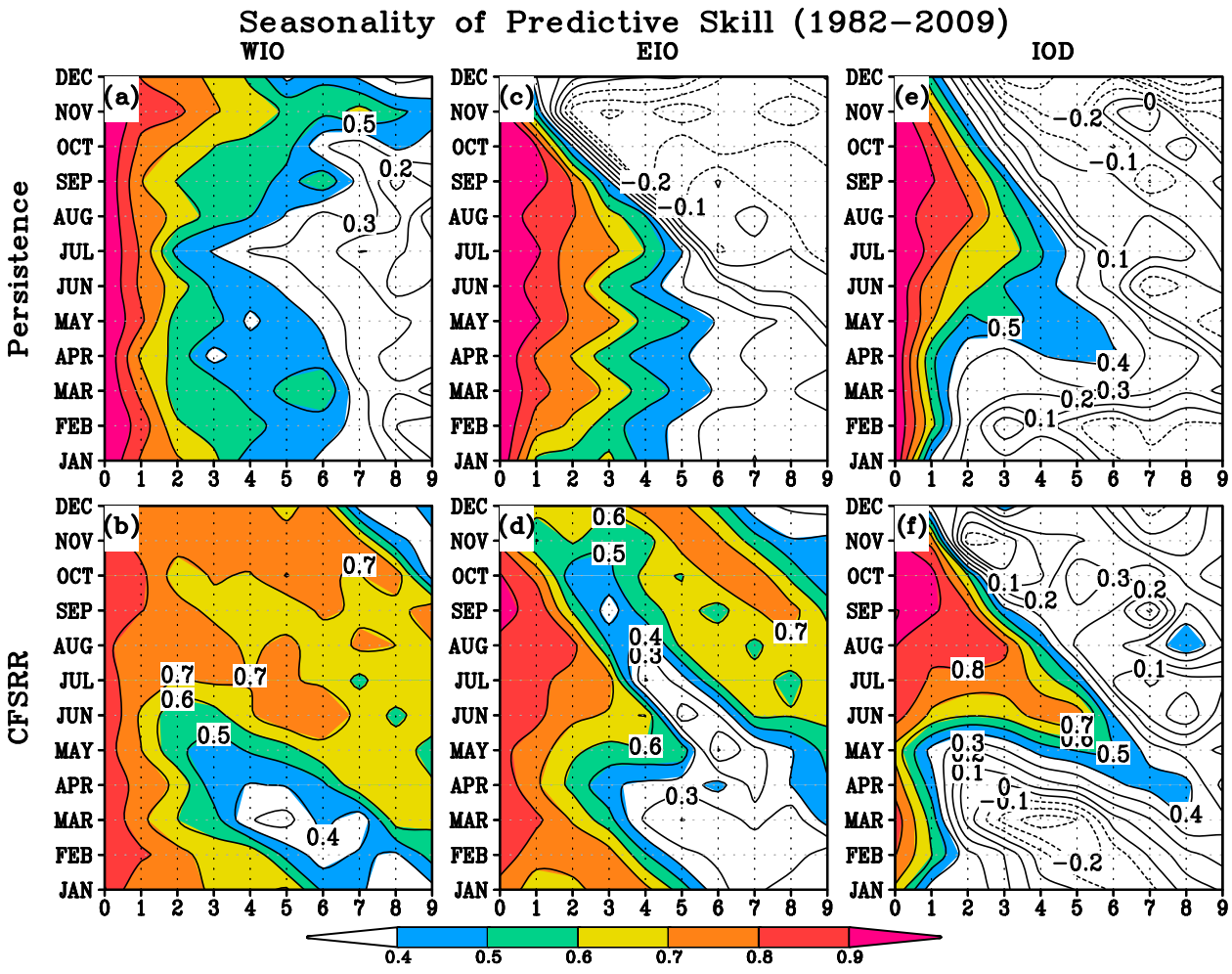

FIG. 5. Prediction skills (anomaly correlation coefficients) as functions of IC months (y axis) and lead months (x axis) for (a),(b) SST anomalies in the WIO (10°S–10°N, 50°–70°E), (c),(d) SST anomalies in the EIO (10°S–0°, 90°–110°E), and (e),(f) the IOD index, based on all predictions during 1982–2009, for (top) persistence and (bottom) CFSRR forecast.

which also looks somewhat different from that for IOD (Fig. 5f). In fact, CFSRR features low skill during boreal summer for both poles (Figs. 5b,d) and around December for EIO (Fig. 5d). The WIO also suffers from a diminution of skill in November but shows high skill in September–October and December–April (Fig. 5b). The most predictable target months for EIO are March–April and, to a lesser extent, September–October. These characteristics show that the relatively high prediction skill in WIO and EIO (Fig. 4) can be mostly attributed to seasons other than the IOD peak season, although the highest IOD skill in September–October (Fig. 5f) corresponds to relatively high skill in both poles (Figs. 5b,d) and likely reflects the genuine tendency for the two poles to be out of phase. On the other hand, the high skill in both poles in March does not yield a corresponding high in IOD skill with leads over two months, possibly because the skillfully predicted SSTA is largely in phase between the east and west. The same reason can also be used to explain why the IOD skill (Fig. 5e) is lower than that of both poles from January to April (Figs. 5a,c) in persistence. In general, Fig. 5 suggests that the boreal spring prediction barrier for forecasts of the IOD index is caused by the spring barrier for both WIO and EIO SSTA, whereas the December prediction barrier for forecasts of the IOD index is mainly due to the December barrier for EIO SSTA.

CFSRR forecasts are superior to persistence in all three indices, demonstrating additional predictability that is realized by the dynamical forecast system. This is partly because a much weaker seasonality is present for the two poles in persistence, which is hard to recognize in the WIO prediction (Fig. 5a) and only subtly apparent in the EIO (Fig. 5c). On the other hand, the SSTA in November in WIO seems to last longest through persistence (Fig. 5a), a feature shared by its CFSRR

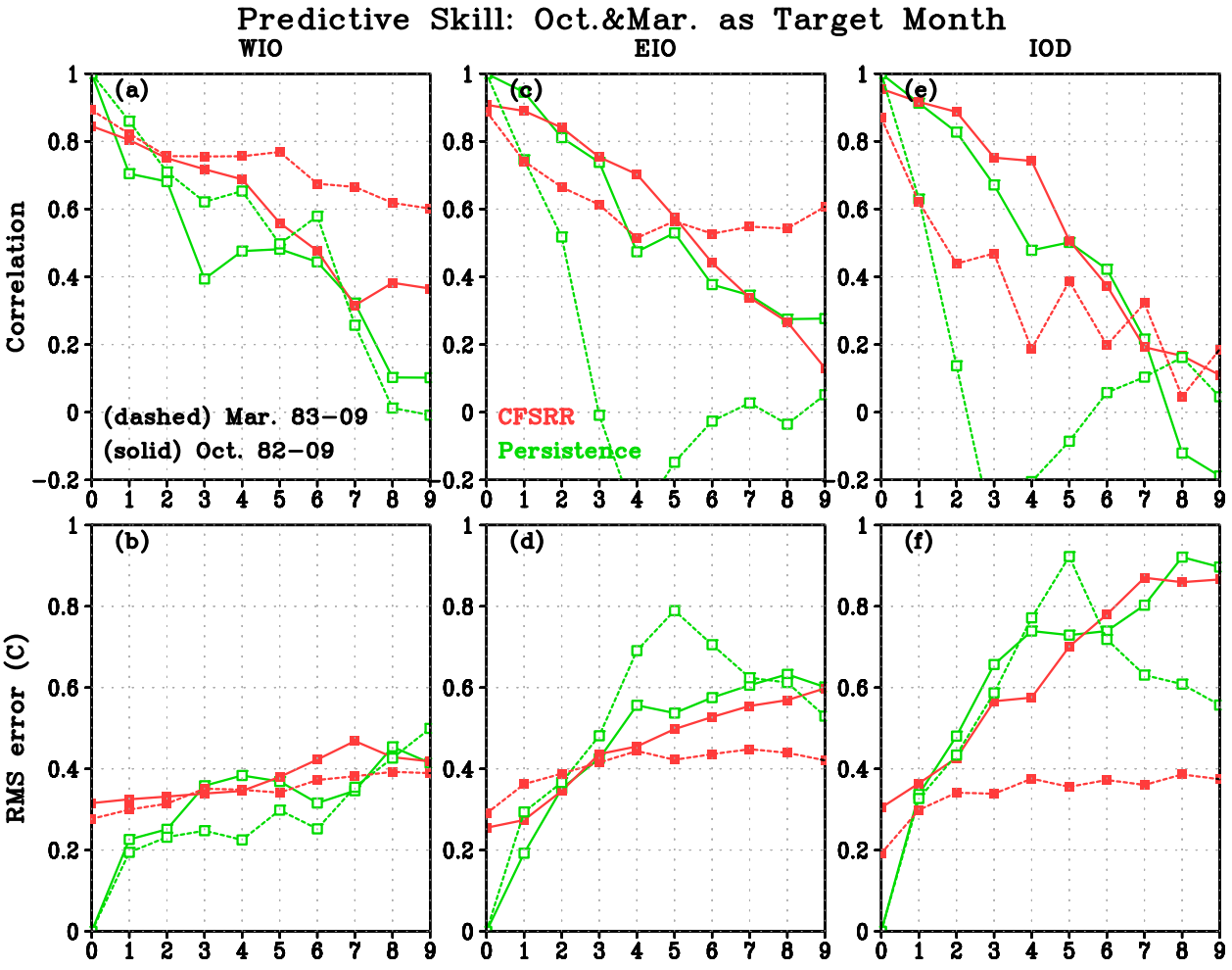

FIG. 6. Predictive skill in target month of October (solid lines) and March (dashed lines). (top) Anomaly correlation coefficients and (bottom) RMS errors (°C) of persistence (green lines) and CFSRR forecast (red lines) as a function of lead months for (a),(b) SST anomalies in the WIO (10°S–10°N, 50°–70°E), (c),(d) SST anomalies in the EIO (10°S–0°, 90°–110°E), and (e),(f) the IOD index. October (March) skill is based on all predictions during 1982–2009 (1983–2009).

counterpart (Fig. 5b). The sharp decay of persistence in November–December (Fig. 5c) in EIO is also shared by the CFSRR (Fig. 5d), which reflects the fast decay of IOD or its quick replacement by the all-basin mode in ENSO years (Huang and Kinter 2002). The model, however, seems to face a stronger spring barrier, especially for WIO.

To further highlight the skill contrast during the IOD season and the season of the basinwide warming mode, Fig. 6 compares the prediction skill of CFSRR and persistence forecasts for all three indices (i.e., WIO, EIO, and IOD) during October with those during March. For WIO, for the anomaly correlation measure (red curves in Fig. 6a), CFSRR clearly has higher skill when predicting March compared to when it is predicting October, with skillful predictions available more than three seasons (less than two seasons) ahead for the former (the latter). The better prediction of WIO during March compared to October is also shown in persistence at lead times of less than 7 months (green curves in Fig. 6a), and a similar difference is found with the RMSE measure (Fig. 6b). Unlike those for WIO, the EIO predictions in CFSRR (red curves in Fig. 6c) do not have consistent differences at all lead times between the two target months, with October (March) forecasts having higher skill at lead times of less (greater) than 5 months for the anomaly correlation measure. For persistence (green curves in Fig. 6c), however, EIO has significantly higher correlation skill for October than March, which may also be true in the RMSE measure (green curves in Fig. 6d). In summary, according to a bulk measure defined as the average anomaly correlation (RMSE) over all 0–9-month leads (Zhu et al. 2012b), in CFSRR the WIO index is generally better predicted for March than

October, but EIO has similar prediction skill for the two target months.

Predictions of IOD index, however, clearly exhibit a different seasonality behavior from the two poles. For the anomaly correlation measure (Fig. 6e), both CFSRR and persistence have higher skill for October compared to March at most lead times (CFSRR can provide skillful predictions longer than one season for the IOD index in October). This feature is again related to the strong seasonality of IOD. In particular, WIO and EIO during October tend to have opposite phases, and the physical basis for the IOD (Saji et al. 1999; Webster et al. 1999) provides potential predictability on the seasonal time scale. In contrast, because of the dominance of the basinwide warming mode during March, WIO and EIO tend to have the same sign and the resulting IOD has relatively low predictability. In practice, however, even for IOD events during October, the present models (e.g., CFSv2) only achieve modest successes in predicting them. For example, according to both anomaly correlation and RMSE measures (solid curves in Figs. 6e,f), CFSRR only slightly outperforms persistence at lead times of shorter than 5 months, even though there seems to be a slight rebound of skill at 8–9-month lead times.

In summary, the above analyses indicate that CFSRR has useful skill predicting the TIO SST, but most of the skill is generally attributable to skill in seasons other than the IOD season. For predictions of the IOD index, there exists a strong seasonality in its prediction skill, with relatively high skill in the boreal autumn. In the following two sections, we further explore the seasonality of the predictability of the TIO SST. In particular, the SST for the whole tropical Indian basin will be treated as single prediction object, and the most predictable pattern will be explored for March and October, respectively.

4. The most predictable SST pattern related to the TIO basinwide warming mode

In this section, the most predictable SST pattern is extracted by applying MSN EOF in the predicted March SSTs at different lead times. As we discussed in section 1, a benefit of the MSN EOF is to determine the most predictable mode in an ensemble of hindcasts objectively and to delineate its spatial pattern naturally without reliance on a priori definitions of the indices.

The MSN EOF is obtained based on the forecast ensemble mean and spread. Each member in an ensemble prediction is treated as equally probable in the MSN EOF calculation, which means that there is no consideration given to the possibility that some members may be better predictions than others. After an MSN EOF mode is determined, its connections with the ocean–atmosphere conditions in the TIO and the tropical Pacific can be obtained for the preceding winter and the contemporary spring by regressing key atmospheric and oceanic fields against the time series associated with the most predictable SST pattern. It should be noted that calculations based on other spring months (i.e., April and May) show quite robust results (figures not shown).

Figure 7 shows the first mode of MSN EOF (MSN EOF1) of the March SSTA in the TIO for (a) March ICs (0-month lead), (b) December ICs (3-month lead), (c) September ICs (6-month lead), and (d) June ICs (9-month lead). The percentages of variance of the ensemble mean SSTA explained by these MSN EOF1 modes are 46.2%, 66.2%, 72.2%, and 75.4% at the four lead times, respectively. There are obvious similarities among the leading patterns for different leads (right panel of Fig. 7), all having a basinwide warming (cooling) in the TIO. The spatial pattern resembles the leading mode of observed SSTA in March (Fig. 1a), even though the loading details are slightly displaced at long lead times. Furthermore, the time series associated with the first MSN EOF modes are also consistent with the one corresponding to EOF1 of observed SSTA in March, with correlations ranging from 0.65 to 0.89 (all above the 95% confidence level). In addition, as seen from the corresponding time series (left panel of Fig. 7), in both observations and hindcasts there is also a long-term warming trend overlaid on the interannual variation during the hindcast period (i.e., 1982–2009), which seems slightly stronger in hindcasts at long lead times than that at 0-month lead time and in observations. This consistency indicates that the observed TIO warming trend, probably attributable to both external forcing and internal variability (Ihara et al. 2008; Du and Xie 2008; Dong et al. 2014), is also reproduced in the CFSv2 hindcasts. Its appearance in hindcasts is at least partially due to the application of historically prescribed (i.e., rising) CO_2 concentrations during the hindcast process (Saha et al. 2014), and probably also associated with the initial conditions. The SST warming trend is relatively well predicted at a lead time of 9 months, but it could be underestimated at longer lead times (e.g., Luo et al. 2011).

Figures 8 and 9 present the anomalous fields of SST, wind stress, and precipitation in the tropical Indian and Pacific Oceans associated with the above MSN EOF1 (Fig. 7) during the preceding winter (e.g., December), corresponding to the peak season of El Niño. The regression patterns for the CFSv2-predicted fields (right column in Figs. 8 and 9) are similar among the four lead times (i.e., 0-, 3-, 6-, and 9-month leads), and they all

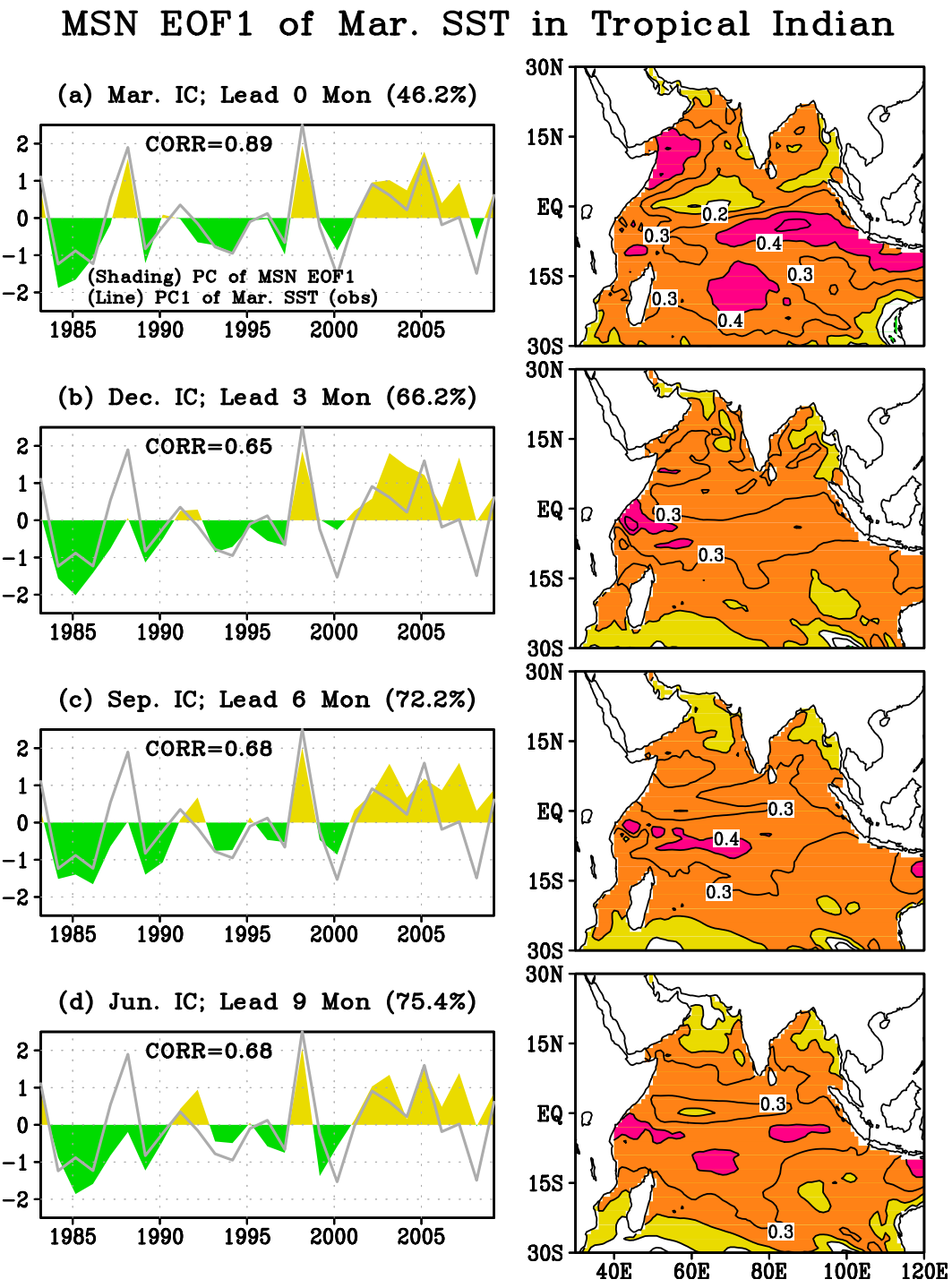

FIG. 7. (left) The normalized time series (color shading) and (right) spatial patterns of MSN EOF1 of the predicted March SSTAs during 1983–2009 at (a) 0-month lead with the March IC, (b) 3-month lead with the preceding December IC, (c) 6-month lead with the preceding September IC, and (d) 9-month lead with the preceding June IC. The contour interval is 0.1°C. The percentage of the explained variance for the ensemble mean anomalies is indicated in each panel. Overlaid in the shading time series is the normalized time series (gray lines) corresponding to EOF1 of observed March SSTA (i.e., Fig. 1a).

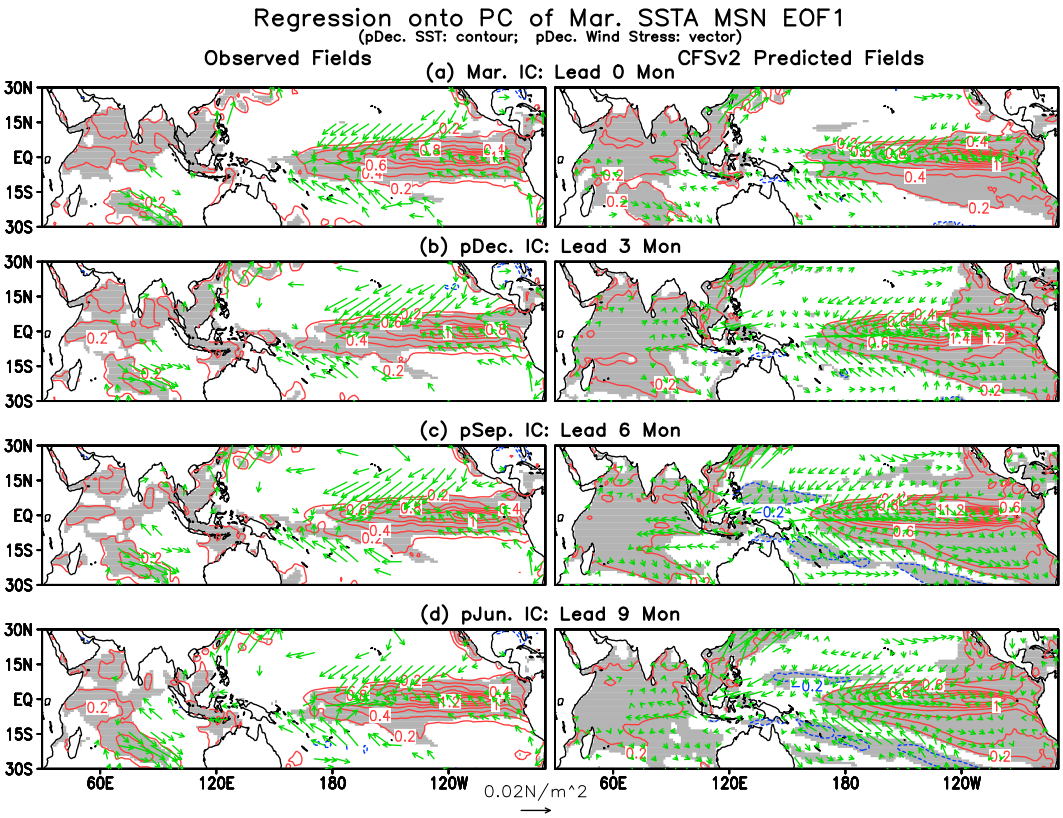

FIG. 8. The regression maps of the (left) observed and (right) predicted anomalous SST (contours, °C) and wind stress (vectors, N m^{-2}) in the preceding December onto the MSE EOF1 time series of predicted March SSTAs at (a) 0-month lead with the March IC (Fig. 7a), (b) 3-month lead with the preceding December IC (Fig. 7b), (c) 6-month lead with the preceding September IC (Fig. 7c), and (d) 9-month lead with the preceding June IC (Fig. 7d). The contour interval for SST is 0.2°C, and the shading is for SST regressions above 95% significance test. Wind stress vectors are shown only if either meridional or zonal wind stress is above 95% significance test.

approximately reproduce those for the observed fields (left column in Figs. 8 and 9), which suggests that the variations associated with MSN EOF1 can be predicted at least 9 months ahead. Also, the regressions are stronger and more significant for the CFSv2-predicted fields (right column in Figs. 8 and 9) than those for the observed fields (left column in Figs. 8 and 9), which might be due to a lower noise level in the former as a result of ensemble averaging.

In the tropical Pacific, in particular, the associated preceding winter patterns in both observations and CFSv2 hindcasts represent a clear El Niño state, which is consistent with previous results that the basin warming mode is induced by El Niño in the tropical Pacific (Nigam and Shen 1993; Klein et al. 1999; Huang and Shukla 2007a; Liu and Alexander 2007; Schott et al. 2009; Kumar et al. 2014). Specifically, the spatial pattern consists of positive SSTAs in the central and eastern tropical Pacific (contours in Fig. 8), anomalous westerlies in the western and central equatorial Pacific accompanied by strong meridional wind convergence from both hemispheres (vectors in Fig. 8), and eastward migration of tropical convection (Fig. 9). Over the tropical northwest Pacific, an anomalous anticyclonic circulation is also evident in all regressions, which is a robust feature associated with El Niño, and through this circulation ENSO exerts influences on the East Asian climate (e.g., Zhang et al. 1996; Wang et al. 2000). On the other hand, there are some subtle differences between the regressions for observations and for hindcasts. For example, as the lead time increases in hindcasts, the meridional extent of SSTAs becomes larger in the eastern tropical Pacific (right column in Fig. 8) and the associated precipitation becomes more symmetric about the equator in the central tropical Pacific (right column in Fig. 9). These differences are related to the CFSv2 biases in representing ENSO and its related atmospheric teleconnections in the tropics, which is confirmed by regressions against the Niño-3.4 index (not shown). The unrealistic symmetric precipitation distribution is likely associated with the double-ITCZ problem in the mean state of CFSv2 (not shown).

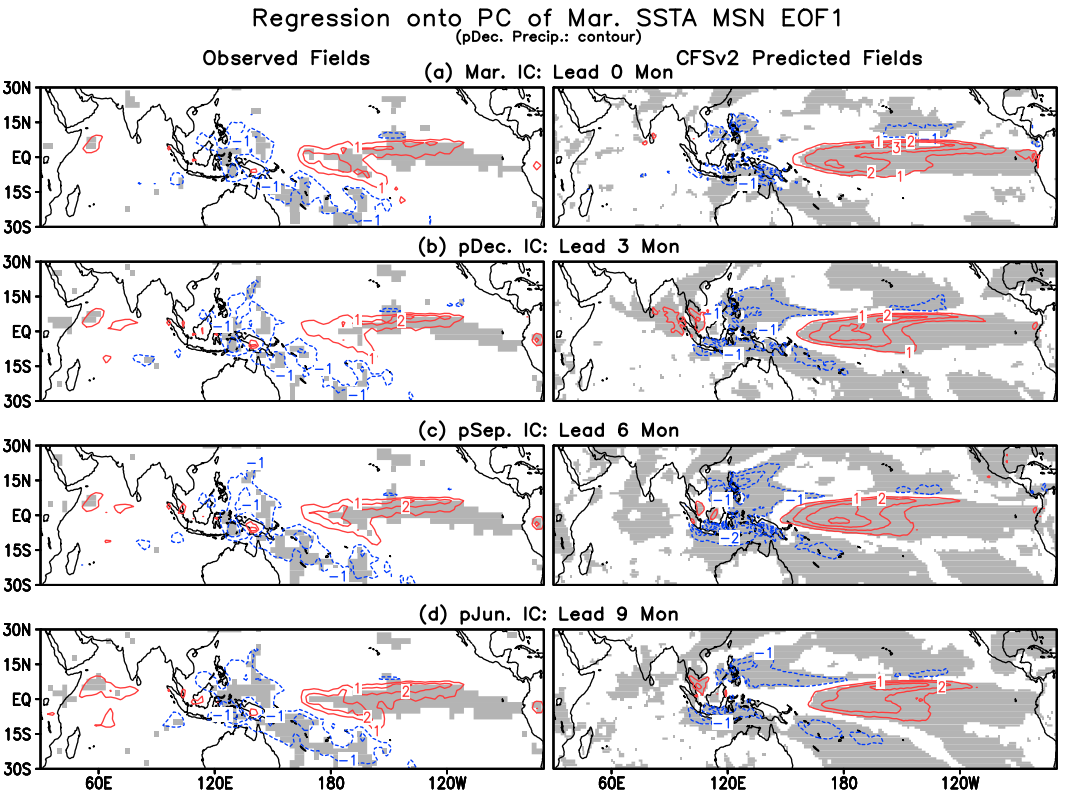

FIG. 9. The regression maps of the (left) observed and (right) anomalous precipitation (contours, mm day^{-1}) in the preceding December onto the MSE EOF1 time series of predicted March SSTAs at (a) 0-month lead with the March IC (Fig. 7a), (b) 3-month lead with the preceding December IC (Fig. 7b), (c) 6-month lead with the preceding September IC (Fig. 7c), and (d) 9-month lead with the preceding June IC (Fig. 7d). The contour interval is 1 mm day^{-1}, and the shading is for precipitation regressions above 90% significance test.

In the TIO, the associated positive SSTA is not evenly distributed around the basin in the preceding winter, as indicated by the regressions for both observations and hindcasts (Fig. 8). Specifically, the northern tropical Indian Ocean generally experiences a uniform warming, which is due to the thermodynamic forcing from El Niño, as a result of reduced cloud cover, for example (e.g., Klein et al. 1999; Chen et al. 2012). The warm SSTA in the central subtropical south Indian Ocean between 15° and 30°S, most prominently in observations (left panels, Fig. 8), is apparently associated with the reduced strength of the southeast trade winds there.

On the other hand, the zonal SSTA contrast is more evident in the southern equatorial Indian Ocean in hindcast regressions, with larger SSTA in the southwestern ocean near Madagascar (right panels, Fig. 8). The zonal difference can be attributed to the persistent effect of the IOD response to El Niño in the region. As will be discussed in the next section, the subsurface temperature anomalies generated in the southeastern equatorial Indian Ocean during the IOD peaks propagate westward and deepen the mean thermocline ridge located in the southwestern Indian Ocean a few months later (e.g., Xie et al. 2002; Huang and Kinter 2002; Huang and Shukla 2007a). Arriving at the western coast in the winter, they contribute to warmer SSTAs in the southwestern Indian Ocean (Fig. 8; Xie et al. 2002; Huang and Kinter 2002). These signals seem to the southwestern region earlier in the model than in observations.

Figures 10 and 11 present the anomalous fields of SST, wind stress, and precipitation in the tropical Indian and Pacific Oceans associated with the above MSN EOF1 (Fig. 7) during the simultaneous spring (e.g., March), corresponding to the decaying season of El Niño. Like those for the antecedent winter (right column in Figs. 8 and 9), the regression patterns for the CFSv2-predicted fields look generally similar. The statistically significant features in both observations and CFSRR are the remnants of ENSO anomalies in the tropical Pacific and the basinwide warming in the Indian Ocean, extending to the western Pacific around the coast of East Asia. The regressions, especially for precipitation, are generally less significant for the observed fields (left column in

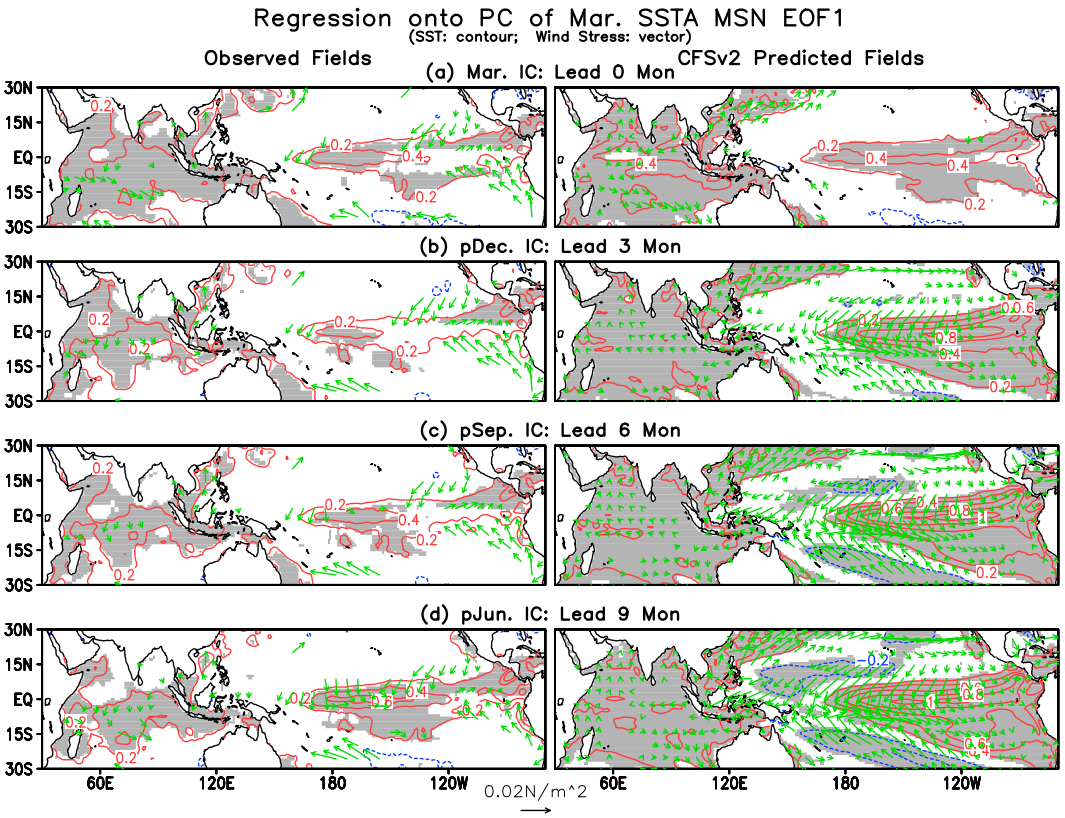

FIG. 10. As in Fig. 8, but for the anomalous SST and wind stress in March.

Figs. 10 and 11), partially due to a higher noise level since the observations represent only one realization.

Compared with the preceding winter (Fig. 8), in both observation- and hindcast-related regressions, the positive SSTAs become generally stronger (and more significant) in the TIO as evidenced by a larger area within the 0.2°C contour, but weaker in the tropical Pacific. In particular, warm signals reach the southwestern Indian Ocean in observations. However, the zonal SSTA difference in the southern equatorial Indian Ocean becomes less evident. According to previous studies (Annamalai et al. 2005; Yang et al. 2007; Xie et al. 2009), different SSTA evolutions in the TIO and tropical Pacific could act to persist the El Niño influences by way of a so-called capacitor effect. That is, the TIO warms in response to El Niño (the charging process), and this warming then influences precipitation in the TIO and surrounding regions after El Niño decays (the discharge process).

In addition, in the tropical Pacific, the decrease of SSTAs from the preceding winter (Fig. 8) to the simultaneous spring (Fig. 10) is more significant in the observed regressions than for the hindcast regressions. This implies a bias in the CFSv2 (i.e., its simulated ENSO persists too long). Also, the anomalous anticyclonic circulation is still evident in the hindcast regressions, especially at 3-, 6- and 9-lead months (right columns of Figs. 10b–d), but it is only subtly present in the observed regressions (left columns of Fig. 10). The difference, once again, is a result of the persistence of ENSO events being different in observations and CFSv2. The bias implies that in CFSv2 the connection between ENSO and the East Asian climate may be unrealistically strong.

In summary, in spring the most predictable SSTA pattern in CFSRR hindcasts is characterized by the TIO basin warming. The predictable mode is closely associated with El Niño in the tropical Pacific. The mode in spring can be predicted at least 9 months ahead. Its associated variations in the preceding winter and the simultaneous spring are also generally captured by CFSv2 nine months ahead, even though some biases are evident.

5. The most predictable pattern related to IOD

In this section, the most predictable SST pattern related to the IOD is extracted by applying the MSN EOF method to the predicted SSTs in October at different lead times, as done above for the basin warming mode. The October SSTA corresponds to the IOD mature phase.

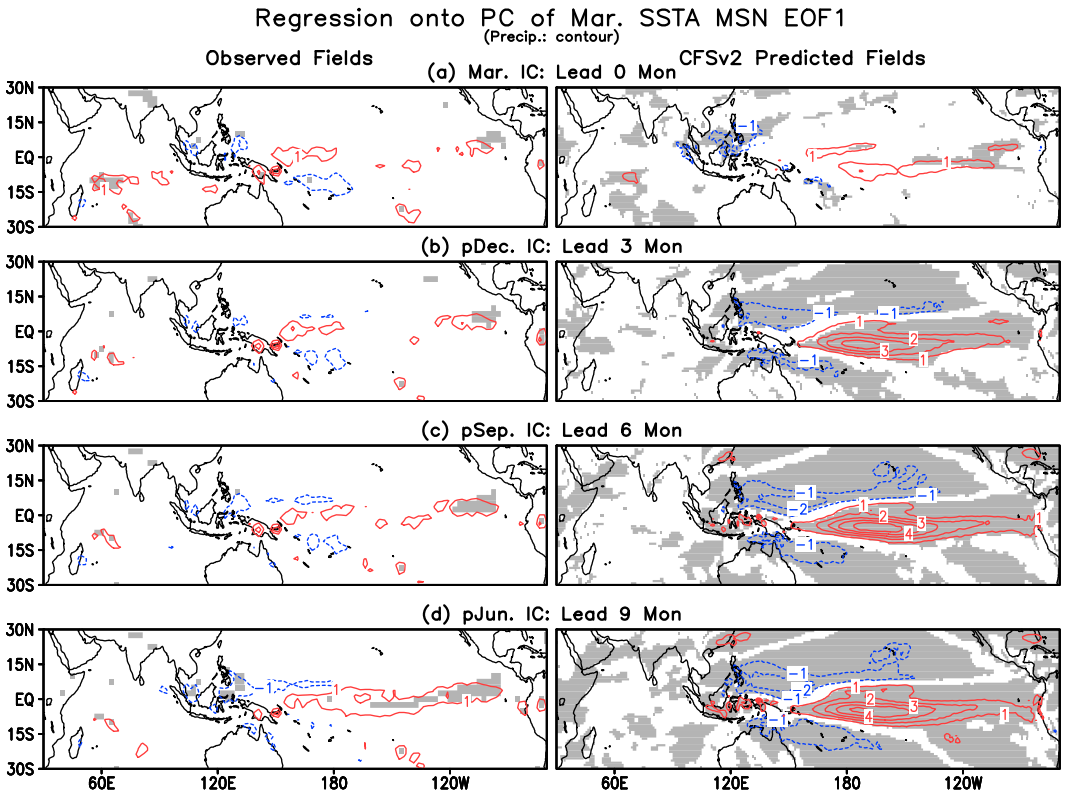

FIG. 11. As in Fig. 9, but for the anomalous precipitation in March.

Figure 12 shows the first mode of MSN EOF (MSN EOF1) of the October SSTA in the TIO for (a) October ICs at a 0-month lead, (b) July ICs at a 3-month lead, (c) April ICs at a 6-month lead, and (d) January ICs at a 9-month lead. The percentages of variance of the ensemble mean SSTA explained by these MSN EOF1 modes are 28.6%, 31.8%, 54.3%, and 25.7% at the four lead times, respectively. There are obvious similarities between the leading patterns derived from the 0- and 3-month lead times (right panel of Figs. 12a,b), which both resemble the leading mode of the observed SSTA in October (Fig. 1b), demonstrating a west–east contrast of SSTAs in the TIO. Also, the time series associated with the MSF EOF1 patterns at 0- and 3-month leads are fairly similar with PC1 of the observed SSTA in October (left panel of Figs. 12a,b), with correlations of 0.81 and 0.66, respectively (both above the 95% confidence level). In addition, the major IOD events, including 1994, 1997, and 2006, were well predicted by CFSv2 at least 3 months ahead.

In contrast to short lead prediction, the prediction skill becomes significantly lower at 6- and 9-month leads (Figs. 12c,d). First, the leading patterns at these lead times start to deviate substantially from the leading mode of the observed SSTA in October (right panel of Figs. 12c,d). In particular, the negative SSTA in the eastern pole become very weak, such that it is hard to recognize at 9-month lead time. Also, there is a clear decline in the consistency between the time series associated with MSN EOF1 and PC1 of the observed SSTA in October (left panel of Figs. 12c,d). The correlation decreases to 0.42 at 6-month lead time and 0.23 at 9-month lead time. In fact, as seen from the associated time series, the major event of 1994 is completely missed by the predictions at both 6- and 9-month lead times. Also, for predictions at the two lead times, the observed SSTA leading pattern in October (Fig. 1b) seems to be better captured by the second MSN EOF mode (not shown), but their associated time series clearly deviate from PC1 of the observed SSTA in October (correlations equal 0.31 and 0.09, respectively).

Figures 13 and 14 show the anomalous fields of SST, wind stress, and precipitation in the tropical Indian and Pacific Oceans associated with the above MSN EOF1 (Fig. 12) during the simultaneous October, which also corresponds to the developing season of El Niño. Because the most predictable mode is not realistically predicted at 6- and 9-month lead times (Fig. 12), the following discussions focus on those at 0- and 3-month lead times. Similar to the basin warming mode, at first

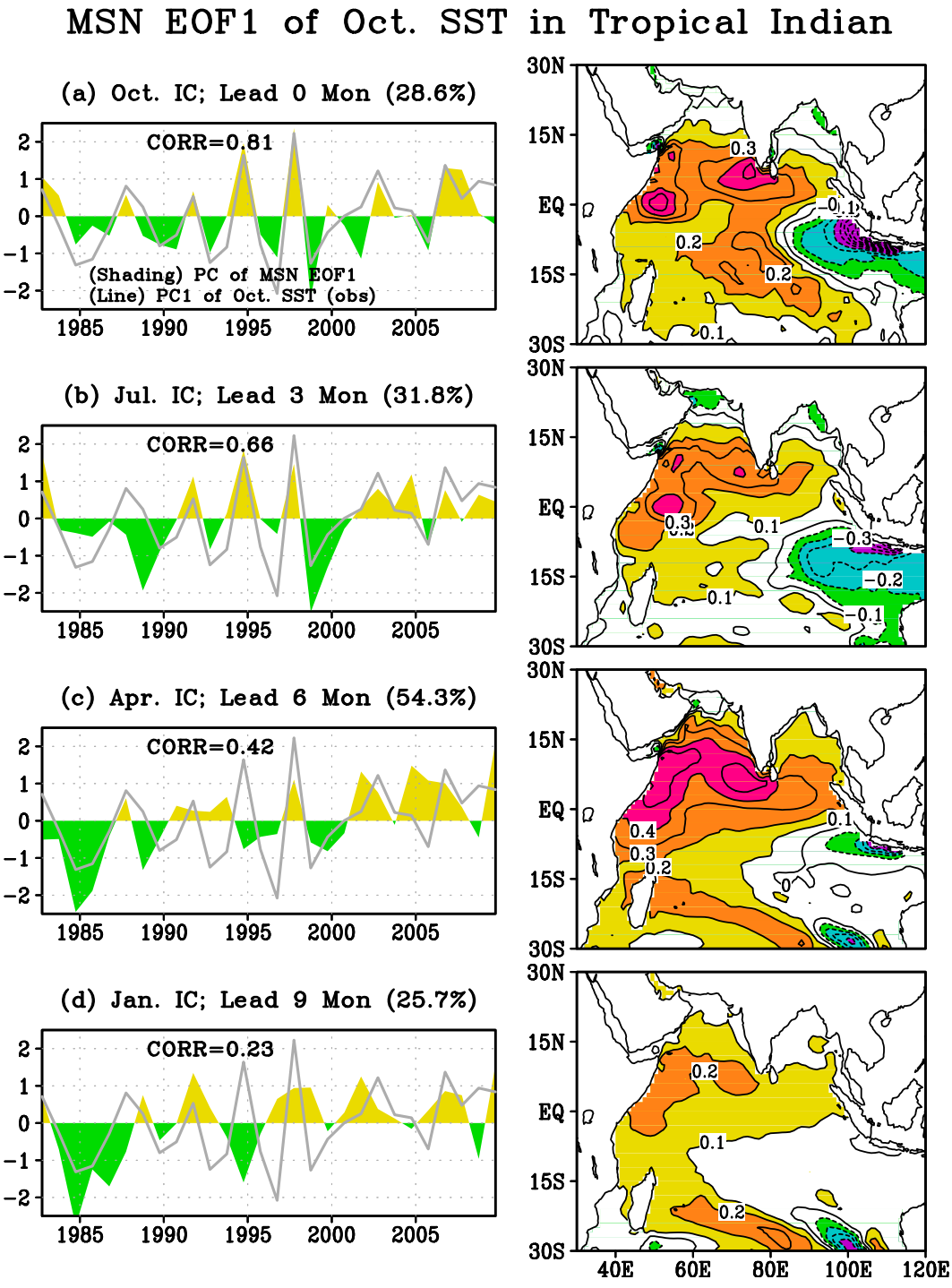

FIG. 12. (left) The normalized time series (color shading) and (right) spatial patterns of MSN EOF1 of the predicted October SSTAs during 1982–2009 at (a) 0-month lead with the October IC, (b) 3-month lead with the July IC, (c) 6-month lead with the April IC, and (d) 9-month lead with the January IC. The contour interval is 0.1°C. The percentage of the explained variance for the ensemble mean anomalies is indicated in each panel. Overlaid in the shading time series is the normalized time series (gray lines) corresponding to EOF1 of observed October SSTA (i.e., Fig. 1b).

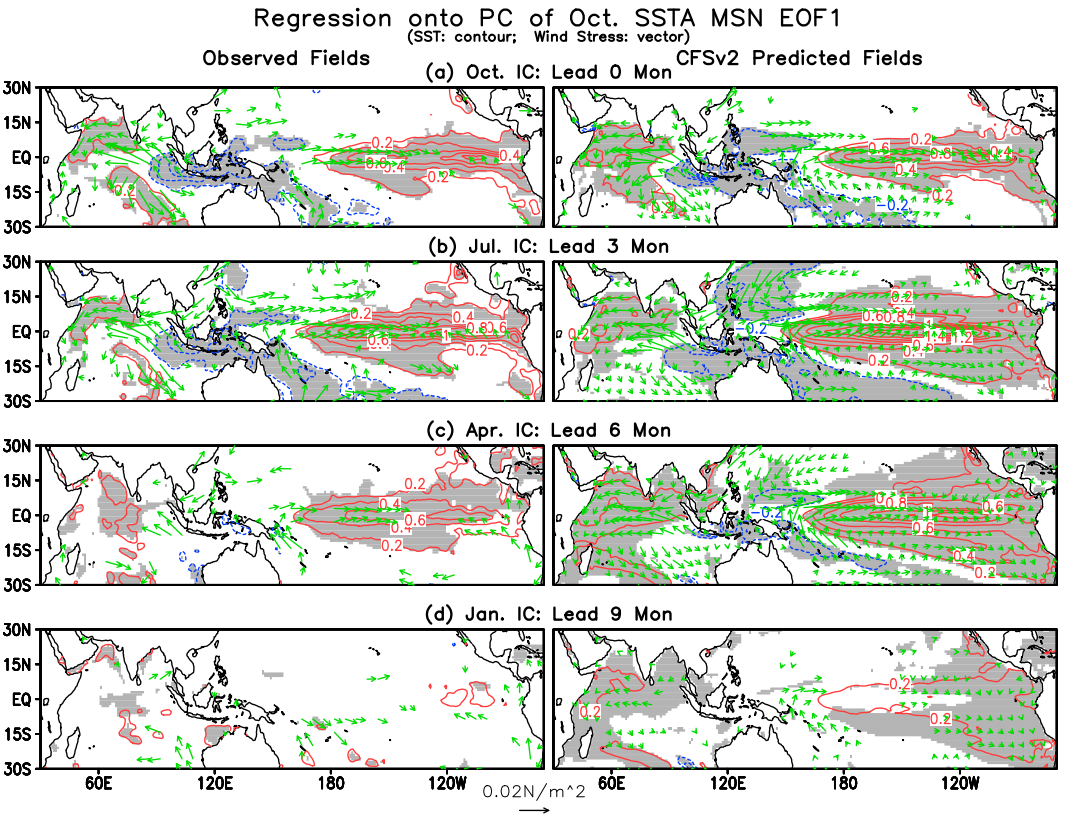

FIG. 13. The regression maps of the (left) observed and (right) predicted anomalous SST (contours, °C) and wind stress (vectors, N m^{-2}) in October onto the MSE EOF1 time series of predicted October SSTAs at (a) 0-month lead with the October IC (Fig. 12a), (b) 3-month lead with the July IC (Fig. 12b), (c) 6-month lead with the April IC (Fig. 12c), and (d) 9-month lead with the January IC (Fig. 12d). The contour interval for SST is 0.2°C, and the shading is for SST regressions above 95% significance test. Wind stress vectors are shown only if either meridional or zonal wind stress is above 95% significance test.

two short lead times the regressions for hindcasts bear a good resemblance to their counterparts in observations, but the former are generally more significant than the latter, which is again due to the fact that there is only one realization in observations but an ensemble of realizations in hindcasts.

In the tropical Pacific, the associated patterns in both observations and hindcasts are again characterized by an El Niño state. However, there are distinct differences between the winds associated with the basin warming mode (Figs. 8 and 10) and those associated with IOD (Fig. 13). In the former, the strong meridional wind convergence from both hemispheres is evident along most longitudes near the equator (Figs. 8 and 10). In contrast, the surface winds associated with IOD (Fig. 13) display larger anomalous westerlies in the western and central equatorial Pacific, but clearly much weaker meridional wind convergence. The difference is due to the different phase relationships with ENSO, with the former (latter) corresponding to the peak and decay (developing) phase of ENSO. The associated winds for the latter act as an active dynamic driver for the tropical Pacific, while in the former they are a response to the ENSO-related SSTA. In addition, the equatorial easterly wind anomalies in the central and eastern Indian Ocean are accompanied by weaker southeast trade winds in central south Indian Ocean. As a result, an anomalous anticyclonic wind curl is established to the south of the equator, which forces significant thermocline deepening in the central part of the southern Indian Ocean around 10°S and generates the subsequent effects discussed in last section.

In the TIO, there are distinct spatial characteristics associated with the IOD. In particular, greater-than-average SST (Fig. 13) and greater precipitation (Fig. 14) appear in the western Indian Ocean region, but the eastern Indian Ocean features by surface cooling (Fig. 13) and a precipitation deficit (Fig. 14). The western and eastern poles are bridged by the anomalous easterlies near the equator (Fig. 13). The pattern can be

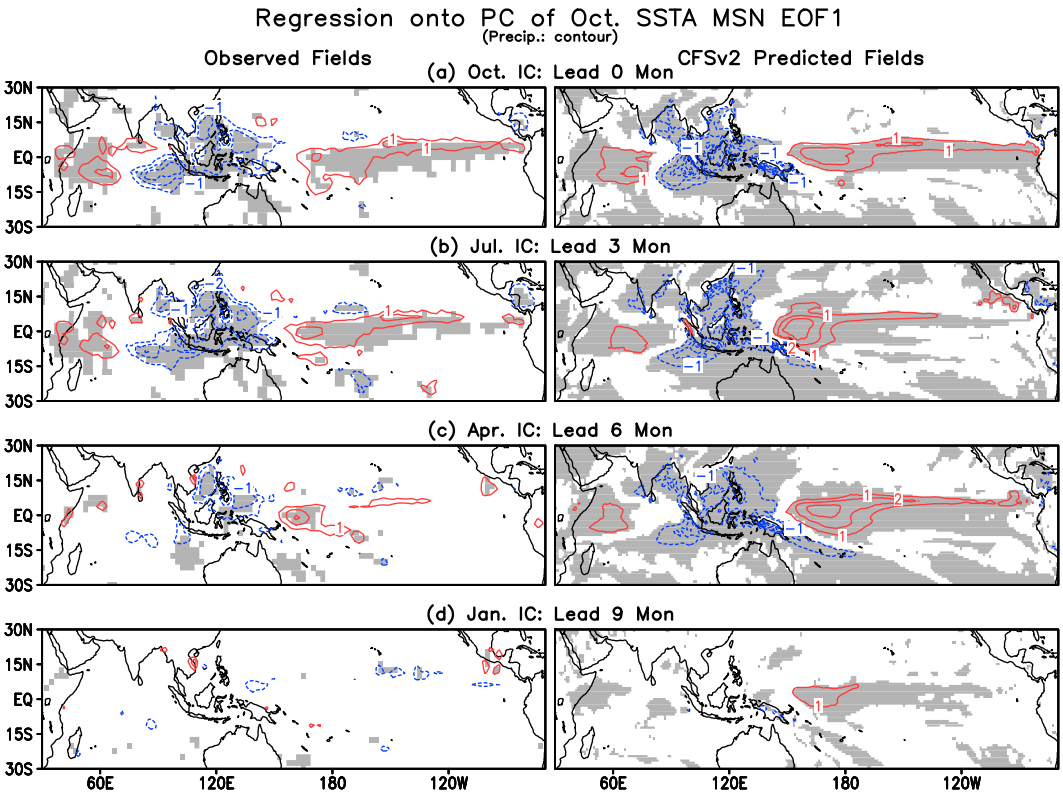

FIG. 14. The regression maps of the (left) observed and (right) anomalous precipitation (contours, mm day^{-1}) in October onto the MSE EOF1 time series of predicted October SSTAs at (a) 0-month lead with the October IC (Fig. 12a), (b) 3-month lead with the July IC (Fig. 12b), (c) 6-month lead with the April IC (Fig. 12c), and (d) 9-month lead with the January IC (Fig. 12d). The contour interval is 1 mm day^{-1}, and the shading is for precipitation regressions above 90% significance test.

triggered by anomalous equatorial easterly anomalies and southeasterlies off Sumatra (not shown; Xie et al. 2002; Huang and Kinter 2002), which induce the coastal and equatorial upwelling around the Sumatra coast, cooling the SST locally. The westward shift of tropical convection fuels the anomalous easterly winds near the equator, consistent with the Bjerknes positive feedback (e.g., Saji et al. 1999).

The coincident appearance of ENSO and IOD suggests a mutual relationship between them, which could be connected by the precipitation deficit extending from the eastern Indian Ocean through the Maritime Continent to the western Pacific (Figs. 14a,b). In particular, IODs can be triggered by El Niño. During the El Niño state, tropical convection migrates eastward to the central Pacific, which results in negative precipitation anomalies in the regions from the eastern Indian Ocean to the western Pacific. The precipitation deficit, in turn, favors easterlies over the equatorial Indian Ocean (Figs. 13a,b), which can trigger a positive IOD. The causal relationship can actually be confirmed by the fact that the present regression patterns (Figs. 13 and 14) are similar to the ones calculated against the Niño-3.4 index in fall (figures not shown). On the other hand, El Niño may also be affected by an IOD in the Indian Ocean (Luo et al. 2010; Izumo et al. 2010). An IOD event can have a significant influence on the ascending branch of the Walker circulation, due to its related variations in SST and precipitation. Specifically, the precipitation deficit in the eastern Indian Ocean (Figs. 14a,b) related to a positive IOD could force equatorial Pacific westerly anomalies in fall (Figs. 13a,b), which could potentially affect the evolution of an ENSO event. However, because of the strong seasonality of ENSO, the influence may be limited, since the winds appear too late to play a major role in initiating an ENSO event.

Even though ENSO and IOD statistically tend to appear simultaneously, not all IOD events co-occur with ENSO. A good example is 1994, when there was a strong IOD event but only a very weak warm pool El Niño. The major 1997 IOD event, in contrast, happened with the strong El Niño state in the Pacific Ocean. Regarding the two major IOD events, some models predict both at 3-month lead (Wajsowicz 2005), while some models predict the

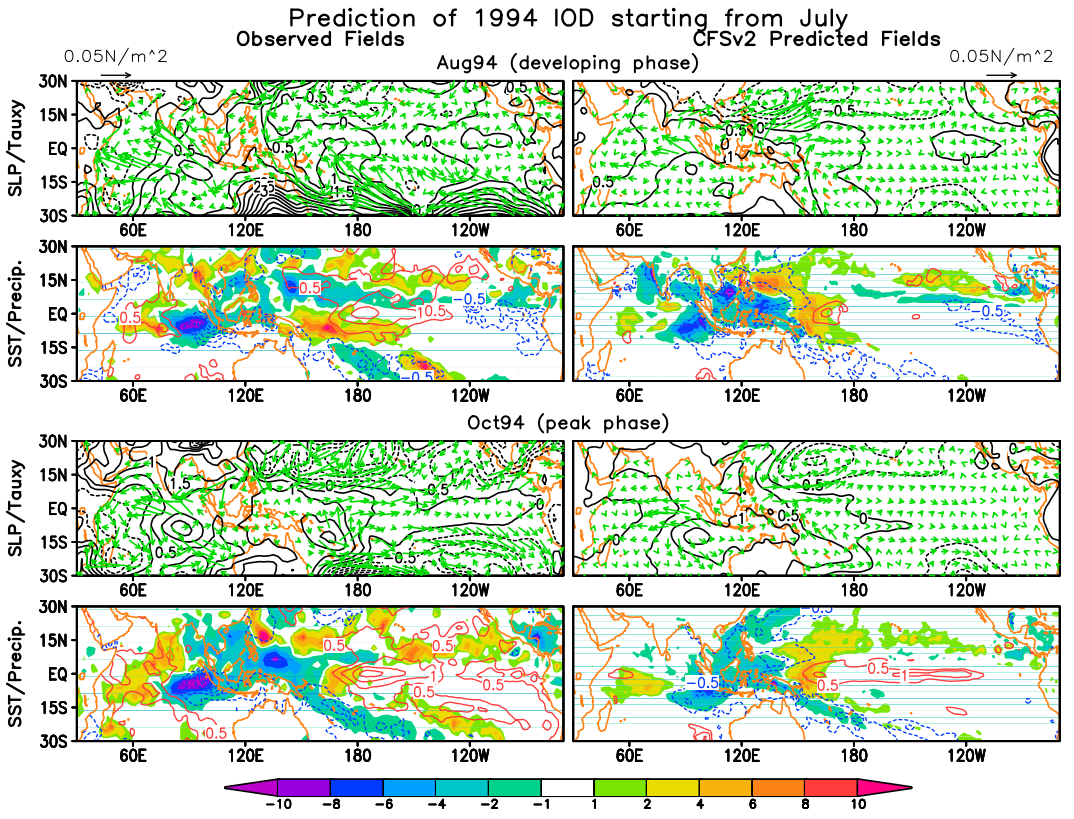

FIG. 15. The 1994 IOD evolution in (left) observations and (right) predictions starting from July 1994. (top) Anomalous sea level pressure (contours, hPa) and surface wind stress (vectors, N m^{-2}) in August 1994 (i.e., developing phase). (second row) Anomalous SST (contours, °C) and precipitation (shading, mm day^{-1}) in August 1994 (i.e., developing phase). (third row) Anomalous sea level pressure (contours, hPa) and surface wind stress (vectors, N m^{-2}) in October 1994 (i.e., peak phase). (bottom) Anomalous SST (contours, °C) and precipitation (shading, mm day^{-1}) in October 1994 (i.e., peak phase). The color bar is for precipitation.

1994 event well but the 1997 event not as well (Luo et al. 2007). Here, we examine the predictions by CFSv2. Figures 15 and 16 respectively present the predictions of the two IOD events, both starting from July initial conditions. By evaluating their peak phase (e.g., October; lower two rows in Figs. 15 and 16), both events seems to be well predicted starting from as early as July (i.e., at a 3-month lead time), but with slightly weaker amplitudes.

We first look at the prediction of the 1994 event in detail. In August (upper two rows in Fig. 15), both observation and CFSv2 have insignificant signals in the tropical Pacific, with minor negative SSTAs in the eastern Pacific and minor positive SSTAs in the western and central Pacific. In observations, there are strong anticyclonic circulations in the southern subtropics, which, however, are absent in CFSv2. The inconsistency suggests that the anticyclones were not vital for the development of the 1994 IOD that was still well predicted by CFSv2.

By contrast, a widespread cyclonic circulation is present in the northwestern Pacific in both observations and CFSv2, accompanied by positive precipitation anomalies around the same region. According to previous studies (e.g., Huang and Shukla 2007b), in the absence of ENSO, the anomalous events in the TIO could be triggered by the anomalous cyclone over the tropical northwestern Pacific. In particular, for the latter a regional direct thermal cell could cause subsidence over the southeastern Indian Ocean. This indeed seems to happen in both observations and CFSv2 as evidenced by an anomalous anticyclonic circulation pattern over the same region. The above meridional structure is more significant in CFSv2, but is slightly distorted in observations probably due to the existence of strong anticyclonic circulations in the southern subtropics. The direct thermal cell, in turn, enhances the southeast trade winds over the southeastern equatorial Indian Ocean, which initiates the IOD development.

Once initiated, the IOD further develop as results of Bjerknes feedback. In August, there is clearly negative SSTA in the eastern TIO, but it is ill organized in

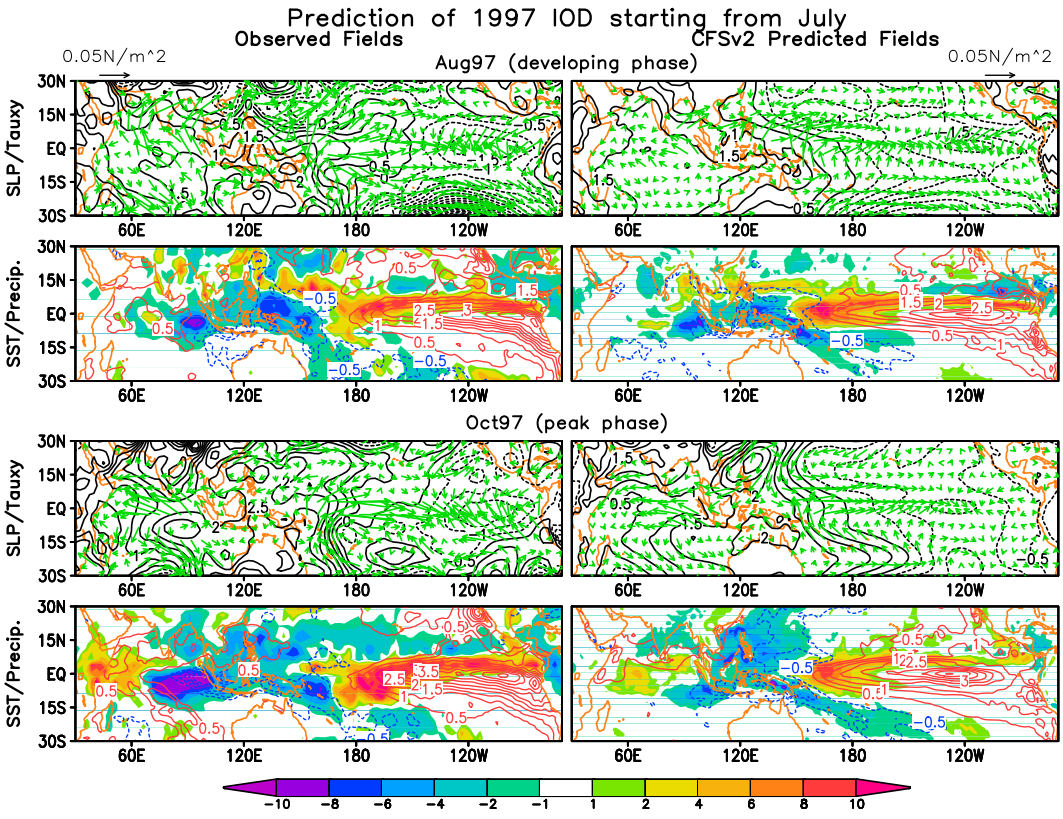

FIG. 16. As in Fig. 15, but for the 1997 IOD event.

the western Indian basin. By October (lower two rows in Fig. 15), the structure of IOD is well developed. The anomalous cyclone over the tropical northwestern Pacific and the anomalous anticyclone over the southeastern Indian Ocean become stronger. The SST and precipitation both have a west–east contrasting structure. Also, in the tropical Pacific, some positive SSTA is present in both observations and CFSv2 hindcast, which is probably a by-product of the IOD development.

For the 1997 event (Fig. 16), the characteristics noted in 1994 are also more or less present, but they are masked by the strong El Niño signal in the Pacific. As a result of the Walker circulation modulation by SSTA in the eastern Pacific, a precipitation deficit extends from the eastern Indian Ocean through the Maritime Continent to the western Pacific, a pattern similar to that derived statistically (Fig. 14). Corresponding to the precipitation deficit, anomalous easterlies are favored over the equatorial Indian Ocean, which could trigger a positive IOD. Once initiated, IOD and ENSO would affect each other in a constructive way (Luo et al. 2010; Izumo et al. 2010), in addition to the developments due to their internal positive Bjerknes feedback.

In summary, the most predictable SSTA pattern in CFSv2 in fall is characterized by the IOD mode, which is consistent with the dominant mode in the observed SSTA in fall. However, the mode can generally be predicted only 1–2 seasons ahead. The associated variations in the same fall season are also generally captured by CFSv2 at the same lead time. Also, the predictable mode statistically tends to coexist with El Niño in the tropical Pacific, but the 1994 event that occurred in the absence of ENSO was also well predicted at least 3 months ahead.

6. Conclusions and discussion

In this study, we explored the seasonality in the predictive skill and the most predictable pattern of the SSTA in the tropical Indian Ocean, by analyzing the hindcasts (1982–2009) using NCEP CFSv2. The most predictable patterns were isolated by an empirical orthogonal function analysis with a maximized signal-to-noise ratio (MSN EOF). The possible connections of these predictable patterns with the conditions in the tropical Pacific were also examined.

As for the overall predictive skill of SSTA in the TIO, CFSv2 generally had useful prediction skill in the

tropical Indian ocean SST compared with persistence. Also, most of the skill is contributed from predictions for seasons other than the IOD season (i.e., the boreal autumn). In another word, the skill was mostly attributed to the TIO basin-warming mode, but is only weakly related to the IOD. The prediction skill of the IOD index exhibited strong seasonality, with relatively high skill in the early boreal autumn. In spite of this, CFSv2 did not have significantly better skill in predicting IOD than persistence.

The seasonality in the predictable patterns of the TIO SST was explored by applying MSN EOF to the predicted SSTA during March and October, respectively. For March, the most predictable pattern was characterized by the basinwide warming in the TIO. The predictable mode was found to be closely associated with El Niño in the tropical Pacific. Also, the basin warming mode in spring, including its associated variations in the preceding winter and the simultaneous spring, can be predicted at least 9 months ahead, even though some biases were evident. On the other hand, the most predictable SSTA pattern in fall is characterized by the IOD mode. The mode, however, was only predicted only 1–2 seasons ahead. CFSv2 also predicted its associated variations in the simultaneous fall at the similar lead time. Statistically, the predictable mode coexisted with El Niño in the tropical Pacific, but there are also cases, like the 1994 event, that occurred in the absence of ENSO. By evaluating their peak phase, both 1994 and 1997 IOD events seem to be well predicted starting from as early as July (i.e., at a 3-month lead time).

We also identified some systematic model biases in CFSv2 (Huang et al. 2007), particularly the ENSO-related biases. For example, in CFSv2 the meridional extent of ENSO-related SSTA was unrealistically large in the eastern tropical Pacific, and the ENSO-related precipitation variations were too symmetric relative to the equator in the central tropical Pacific. The latter was likely associated with the double-ITCZ problem in the mean state of CFSv2. Also, the ENSO-related SSTA in the eastern tropical Pacific persisted too long, which might result in a stronger connection between ENSO and the East Asian climate than in observations. Further sensitivity experiments, similar to those by Huang and Shukla (2007a,b), are required to evaluate how robust the relationships described in this paper are in CFSv2, which will be examined in the future.

Acknowledgments. Funding for this study is provided by grants from NSF (ATM-0830068), NOAA (NA09OAR4310058), and NASA (NNX09AN50G).

APPENDIX

A Brief Introduction to EOF Analysis with Maximized Signal-To-Noise Ratio (MSN EOF)

The MSN EOF employed here follows Venzke et al. (1999) and Huang (2004). In a finite ensemble, the ensemble mean is composed of a true forced and a random part (i.e., $\mathbf{X}_M = \mathbf{X}_F + \mathbf{X}_R$; the bold letters represent matrices or vectors). The MSN EOF method optimally estimates the dominant pattern of $\mathbf{X}_F$ in the presence of $\mathbf{X}_R$. If $\mathbf{X}_F$ and $\mathbf{X}_R$ are temporally uncorrelated with each other, the covariance matrix of $\mathbf{X}_M$ can be separated into forced and a residual noise covariance matrices (i.e., $\mathbf{C}_M = \mathbf{C}_F + \mathbf{C}_R$). To find the eigenvectors of $\mathbf{C}_F$, the key procedure is to eliminate the spatial covariance of noise, which, mathematically, is equivalent to finding a transformation $\mathbf{F}$ such that $\mathbf{F}^{\mathrm{T}}\mathbf{C}_R\mathbf{F} = \mathbf{I}$ ($\mathbf{I}$ is identity matrix). This procedure is referred to as a ''prewhitening'' transformation, because the internal variations become spatial white noise by the transformed matrix, which guarantees that $\mathbf{F}^{\mathrm{T}}\mathbf{C}_F\mathbf{F}$ and $\mathbf{F}^{\mathrm{T}}\mathbf{C}_M\mathbf{F}$ have identical eigenvalues.

In practice, $\mathbf{F}$ is estimated from the first K weighted EOF patterns of the deviations $\mathbf{X}'_i = \mathbf{X}_i - \mathbf{X}_M$, where i denotes the ith member within the ensemble. The matrix of eigenvectors ($\mathbf{E}$) of $\mathbf{F}^{\mathrm{T}}\mathbf{C}_M\mathbf{F}$ contains a set of noise filters, which can be restored into physical space by $\tilde{\mathbf{E}} = \mathbf{FE}$. The optimal filter $\tilde{\mathbf{e}}$ (i.e., the first column vector of $\tilde{\mathbf{E}}$) maximizes the ratio of the variances of the ensemble mean and within-ensemble deviations. The optimally filtered time series of $\mathbf{X}_M$ (i.e., its projection onto $\tilde{\mathbf{e}}$) gives the first MSN principal component (PC).

REFERENCES

Allen, M. R., and L. A. Smith, 1997: Optimal filtering in singular spectrum analysis. *Phys. Lett.*, **234A**, 419–428, doi:10.1016/S0375-9601(97)00559-8.

Annamalai, H., P. Liu, and S.-P. Xie, 2005: Southwest Indian Ocean SST variability: Its local effect and remote influence on Asian monsoons. *J. Climate*, **18**, 4150–4167, doi:10.1175/JCLI3533.1.

Baquero-Bernal, A., M. Latif, and S. Legutke, 2002: On dipolelike variability of sea surface temperature in the tropical Indian Ocean. *J. Climate*, **15**, 1358–1368, doi:10.1175/1520-0442(2002)015<1358:ODVOSS>2.0.CO;2.

Cai, W., P. V. Rensch, T. Cowan, and H. H. Hendon, 2011: Teleconnection pathways of ENSO and the IOD and the mechanism for impacts on Australian rainfall. *J. Climate*, **24**, 3910–3923, doi:10.1175/2011JCLI4129.1.

Cane, M. A., S. E. Zebiak, and S. C. Dolan, 1986: Experimental forecast of El Niño, *Nature*, **321**, 827–832, doi:10.1038/321827a0.

Chang, P., R. Saravanan, L. Ji, and G. C. Hegerl, 2000: The effect of local sea surface temperatures on atmospheric circulation over the tropical Atlantic sector. *J. Climate*, **13**, 2195–2216, doi:10.1175/1520-0442(2000)013<2195:TEOLSS>2.0.CO;2.

Charney, J. G., and J. Shukla, 1981: Predictability of monsoons. *Monsoon Dynamics*, J. Lighthill and R. P. Pearce, Eds., Cambridge University Press, 99–109.

Chen, M., W. Wang, A. Kumar, H. Wang, and B. Jha, 2012: Ocean surface impacts on the seasonal precipitation over the tropical Indian Ocean. *J. Climate*, **25**, 3566–3582, doi:10.1175/JCLI-D-11-00318.1.

Clark, C., P. Webster, and J. Cole, 2003: Interdecadal variability of the relationship between the Indian Ocean zonal mode and East African coastal rainfall anomalies. *J. Climate*, **16**, 548–554, doi:10.1175/1520-0442(2003)016<0548:IVOTRB>2.0.CO;2.

Dong, L., T. Zhou, and B. Wu, 2014: Indian Ocean warming during 1958–2004 simulated by a climate system model and its mechanism. *Climate Dyn.*, **42**, 203–217, doi:10.1007/s00382-013-1722-z.

Du, Y., and S. P. Xie, 2008: Role of atmospheric adjustments in the tropical Indian Ocean warming during the 20th century in climate models. *Geophys. Res. Lett.*, **35**, L08712, doi:10.1029/2008GL033631.

Feng, R., W. Duan, and M. Mu, 2014: The ''winter predictability barrier'' for IOD events and its error growth dynamics: Results from a fully coupled GCM. *J. Geophys. Res. Oceans*, **119**, 8688–8708, doi:10.1002/2014JC010473.

Guan, Y., J. Zhu, B. Huang, Z.-Z. Hu, and J. L. Kinter III, 2014: South Pacific Ocean dipole: A predictable mode on multi-seasonal time scales. *J. Climate*, **27**, 1648–1658, doi:10.1175/JCLI-D-13-00293.1.

Guan, Z., and T. Yamagata, 2003: The unusual summer of 1994 in East Asia: IOD teleconnections. *Geophys. Res. Lett.*, **30**, 1544, doi:10.1029/2002GL016831.

Hastenrath, S., and L. Heller, 1977: Dynamics of climatic hazards in northeast Brazil. *Quart. J. Roy. Meteor. Soc.*, **103**, 77–92, doi:10.1002/qj.49710343505.

Hoerling, M. P., and A. Kumar, 2002: Atmospheric response patterns associated with tropical forcing. *J. Climate*, **15**, 2184–2203, doi:10.1175/1520-0442(2002)015<2184:ARPAWT>2.0.CO;2.

Hu, Z.-Z., and B. Huang, 2007: The predictive skill and the most predictable pattern in the tropical Atlantic: The effect of ENSO. *Mon. Wea. Rev.*, **135**, 1786–1806, doi:10.1175/MWR3393.1.

——, A. Kumar, B. Huang, W. Wang, J. Zhu, and C. Wen, 2013: Prediction skill of monthly SST in the North Atlantic Ocean in NCEP Climate Forecast System version 2. *Climate Dyn.*, **40**, 2745–2756, doi:10.1007/s00382-012-1431-z.

——, ——, ——, J. Zhu, and Y. Guan, 2014: Prediction skill of North Pacific variability in NCEP Climate Forecast System version 2: Impact of ENSO and beyond. *J. Climate*, **27**, 4263–4272, doi:10.1175/JCLI-D-13-00633.1.

Huang, B., 2004: Remotely forced variability in the tropical Atlantic Ocean. *Climate Dyn.*, **23**, 133–152, doi:10.1007/s00382-004-0443-8.

——, and J. L. Kinter III, 2002: Interannual variability in the tropical Indian Ocean. *J. Geophys. Res.*, **107**, 3199, doi:10.1029/2001JC001278.

——, and J. Shukla, 2007a: Mechanisms for the interannual variability in the tropical Indian Ocean. Part I: The role of remote forcing from the tropical Pacific. *J. Climate*, **20**, 2917–2936, doi:10.1175/JCLI4151.1.

——, and ——, 2007b: Mechanisms for the interannual variability in the tropical Indian Ocean. Part II: Regional processes. *J. Climate*, **20**, 2937–2960, doi:10.1175/JCLI4169.1.

——, Z.-Z. Hu, and B. Jha, 2007: Evolution of model systematic errors in the tropical Atlantic basin from the NCEP coupled hindcasts. *Climate Dyn.*, **28**, 661–682, doi:10.1007/s00382-006-0223-8.

Ihara, C., Y. Kushnir, and M. A. Cane, 2008: Warming trend of the Indian Ocean SST and Indian Ocean dipole from 1880 to 2004. *J. Climate*, **21**, 2035–2046, doi:10.1175/2007JCLI1945.1.

Izumo, T., and Coauthors, 2010: Influence of the state of the Indian Ocean dipole on following year's El Niño. *Nat. Geosci.*, **3**, 168–172, doi:10.1038/ngeo760.

Jiang, X., S. Yang, J. Li, Y. Li, H. Hu, and Y. Lian, 2013: Variability of the Indian Ocean SST and its possible impact on summer western North Pacific anticyclone in the NCEP Climate Forecast System. *Climate Dyn.*, **41**, 2199–2212, doi:10.1007/s00382-013-1934-2.

Jin, E. K., and Coauthors, 2008: Current status of ENSO prediction skill in coupled ocean–atmosphere models. *Climate Dyn.*, **31**, 647–664, doi:10.1007/s00382-008-0397-3.

Kanamitsu, M., W. Ebisuzaki, J. Woollen, S.-K. Yang, J. J. Hnilo, M. Fiorino, and G. L. Potter, 2002: NCEP–DOE AMIP-II Reanalysis (R-2). *Bull. Amer. Meteor. Soc.*, **83**, 1631–1643, doi:10.1175/BAMS-83-11-1631.

Klein, S. A., B. J. Soden, and N.-C. Lau, 1999: Remote sea surface temperature variations during ENSO: Evidence for a tropical atmospheric bridge. *J. Climate*, **12**, 917–932, doi:10.1175/1520-0442(1999)012<0917:RSSTVD>2.0.CO;2.

Kug, J.-S., I.-S. Kang, J.-Y. Lee, and J.-G. Jhun, 2004: A statistical approach to Indian Ocean sea surface temperature prediction using a dynamical ENSO prediction. *Geophys. Res. Lett.*, **31**, L09212, doi:10.1029/2003GL019209.

Kumar, A., B. Jha, and H. Wang, 2014: Attribution of SST variability in global oceans and the role of ENSO. *Climate Dyn.*, **43**, 209–220, doi:10.1007/s00382-013-1865-y.

Lamb, P. J., 1978: Large-scale tropical Atlantic surface circulation patterns associated with Subsaharan weather anomalies. *Tellus*, **30**, 240–251, doi:10.1111/j.2153-3490.1978.tb00839.x.

Lau, N.-C., and M. Nath, 2003: Atmosphere–ocean variations in the Indo-Pacific sector during ENSO episodes. *J. Climate*, **16**, 3–20, doi:10.1175/1520-0442(2003)016<0003:AOVITI>2.0.CO;2.

Liu, Z., and M. Alexander, 2007: Atmospheric bridge, oceanic tunnel, and global climatic teleconnections. *Rev. Geophys.*, **45**, RG2005, doi:10.1029/2005RG000172.

Luo, J.-J., S. Masson, S. Behera, S. Shingu, and T. Yamagata, 2005: Seasonal climate predictability in a coupled OAGCM using a different approach for ensemble forecasts. *J. Climate*, **18**, 4474–4497, doi:10.1175/JCLI3526.1.

——, ——, S. K. Behera, and T. Yamagata, 2007: Experimental forecasts of the Indian Ocean dipole using a coupled OAGCM. *J. Climate*, **20**, 2178–2190, doi:10.1175/JCLI4132.1.

——, S. Behera, Y. Masumoto, H. Sakuma, and T. Yamagata, 2008: Successful prediction of the consecutive IOD in 2006 and 2007. *Geophys. Res. Lett.*, **35**, L14S02, doi:10.1029/2007GL032793.

——, R. Zhang, S. K. Behera, Y. Masumoto, F.-F. Jin, R. Lukas, and T. Yamagata, 2010: Interaction between El Niño and extreme Indian Ocean dipole. *J. Climate*, **23**, 726–742, doi:10.1175/2009JCLI3104.1.

——, S. Behera, Y. Masumoto, and T. Yamagata, 2011: Impact of global ocean surface warming on seasonal-to-interannual climate prediction. *J. Climate*, **24**, 1626–1646, doi:10.1175/2010JCLI3645.1.

——, W. Sasaki, and Y. Masumoto, 2012: Indian Ocean warming modulates Pacific climate change. *Proc. Natl. Acad. Sci. USA*, **109**, 18 701–18 706, doi:10.1073/pnas.1210239109.

Nicholls, N., 1989: Sea surface temperatures and Australian winter rainfall. *J. Climate*, **2**, 965–973, doi:10.1175/1520-0442(1989)002<0965:SSTAAW>2.0.CO;2.

Nigam, S., and H. S. Shen, 1993: Structure of oceanic and atmospheric low-frequency variability over the tropical Pacific and Indian Oceans. Part I: COADS observations. *J. Climate*, **6**, 657–676, doi:10.1175/1520-0442(1993)006<0657:SOOAAL>2.0.CO;2.

Reynolds, R. W., N. A. Rayner, T. M. Smith, D. C. Stokes, and W. Wang, 2002: An improved in situ and satellite SST analysis for climate. *J. Climate*, **15**, 1609–1625, doi:10.1175/1520-0442(2002)015<1609:AIISAS>2.0.CO;2.

Saha, S., and Coauthors, 2010: The NCEP Climate Forecast System Reanalysis. *Bull. Amer. Meteor. Soc.*, **91**, 1015–1057, doi:10.1175/2010BAMS3001.1.

——, and Coauthors, 2014: The NCEP Climate Forecast System version 2. *J. Climate*, **27**, 2185–2208, doi:10.1175/JCLI-D-12-00823.1.

Saji, N. H., B. N. Goswami, P. N. Vinayachandran, and T. Yamagata, 1999: A dipole in the tropical Indian Ocean. *Nature*, **401**, 360–363.

Schott, F. A., S.-P. Xie, and J. P. McCreary Jr., 2009: Indian Ocean circulation and climate variability. *Rev. Geophys.*, **47**, RG1002, doi:10.1029/2007RG000245.

Shi, L., H. H. Hendon, O. Alves, J.-J. Luo, M. Balmaseda, and D. Anderson, 2012: How predictable is the Indian Ocean dipole? *Mon. Wea. Rev.*, **140**, 3867–3884, doi:10.1175/MWR-D-12-00001.1.

Song, Q., G. A. Vecchi, and A. J. Rosati, 2008: Predictability of the Indian Ocean sea surface temperature anomalies in the GFDL coupled model. *Geophys. Res. Lett.*, **35**, L02701, doi:10.1029/2007GL031966.

Stockdale, T. N., M. A. Balmaseda, and A. Vidard, 2006: Tropical Atlantic SST prediction with coupled ocean–atmosphere GCMS. *J. Climate*, **19**, 6047–6061, doi:10.1175/JCLI3947.1.

Sutton, R. T., S. P. Jewson, and D. P. Rowell, 2000: The elements of climate variability in the tropical Atlantic region. *J. Climate*, **13**, 3261–3284, doi:10.1175/1520-0442(2000)013<3261:TEOCVI>2.0.CO;2.

Trenberth, K. E., G. W. Branstator, D. Karoly, A. Kumar, N.-C. Lau, and C. Ropelewski, 1998: Progress during TOGA in understanding and modeling global teleconnections associated with tropical sea surface temperatures. *J. Geophys. Res.*, **103**, 14 291–14 324, doi:10.1029/97JC01444.

Venzke, S., M. R. Allen, R. T. Sutton, and D. P. Rowell, 1999: The atmospheric response over the North Atlantic to decadal changes in sea surface temperature. *J. Climate*, **12**, 2562–2584, doi:10.1175/1520-0442(1999)012<2562:TAROTN>2.0.CO;2.

Wajsowicz, R. C., 2005: Potential predictability of tropical Indian Ocean SST anomalies. *Geophys. Res. Lett.*, **32**, L24702, doi:10.1029/2005GL024169.

——, 2007: Seasonal-to-interannual forecasting of tropical Indian Ocean sea surface temperature anomalies: Potential predictability and barriers. *J. Climate*, **20**, 3320–3343, doi:10.1175/JCLI4162.1.

Wang, B., R. Wu, and X. Fu, 2000: Pacific–East Asia teleconnection: How does ENSO affect East Asian climate? *J. Climate*, **13**, 1517–1536, doi:10.1175/1520-0442(2000)013<1517:PEATHD>2.0.CO;2.

Webster, P. J., A. M. Moore, J. P. Loschnigg, and R. R. Leben, 1999: Coupled oceanic–atmospheric dynamics in the Indian Ocean during 1997–98. *Nature*, **401**, 356–360, doi:10.1038/43848.

Wyrtki, K., 1973: An equatorial jet in the Indian Ocean. *Science*, **181**, 262–264, doi:10.1126/science.181.4096.262.

Xie, P., and P. Arkin, 1997: Global precipitation: A 17-year monthly analysis based on gauge observations, satellite estimates, and numerical model outputs. *Bull. Amer. Meteor. Soc.*, **78**, 2539–2558, doi:10.1175/1520-0477(1997)078<2539:GPAYMA>2.0.CO;2.

Xie, S.-P., H. Annamalai, F. Schott, and J. P. McCreary Jr., 2002: Structure and mechanism of South Indian Ocean climate variability. *J. Climate*, **15**, 864–878, doi:10.1175/1520-0442(2002)015<0864:SAMOSI>2.0.CO;2.

——, K. Hu, J. Hafner, H. Tokinaga, Y. Du, G. Huang, and T. Sampe, 2009: Indian Ocean capacitor effect on Indo-western Pacific climate during the summer following El Niño. *J. Climate*, **22**, 730–747, doi:10.1175/2008JCLI2544.1.

Xue, Y., M. Chen, A. Kumar, Z.-Z. Hu, and W. Wang, 2013: Prediction skill and bias of tropical Pacific sea surface temperatures in the NCEP Climate Forecast System version 2. *J. Climate*, **26**, 5358–5378, doi:10.1175/JCLI-D-12-00600.1.

Yang, J., Q. Liu, S.-P. Xie, Z. Liu, and L. Wu, 2007: Impact of the Indian Ocean SST basin mode on the Asian summer monsoon. *Geophys. Res. Lett.*, **34**, L02708, doi:10.1029/2006GL028571.

Zhang, R., A. Sumi, and M. Kimoto, 1996: Impact of El Niño on the East Asian monsoon: A diagnostic study of the '86/87 and '91/92 events. *J. Meteor. Soc. Japan*, **74**, 49–62.

Zhao, M., and H. H. Hendon, 2009: Representation and prediction of the Indian Ocean dipole in the POAMA seasonal forecast model. *Quart. J. Roy. Meteor. Soc.*, **135**, 337–352, doi:10.1002/qj.370.

Zhu, J., and J. Shukla, 2013: The role of air–sea coupling in seasonal prediction of Asian–Pacific summer monsoon rainfall. *J. Climate*, **26**, 5689–5697, doi:10.1175/JCLI-D-13-00190.1.

——, B. Huang, and M. A. Balmaseda, 2012a: An ensemble estimation of the variability of upper-ocean heat content over the tropical Atlantic Ocean with multi-ocean reanalysis products. *Climate Dyn.*, **39**, 1001–1020, doi:10.1007/s00382-011-1189-8.

——, ——, L. Marx, J. L. Kinter III, M. A. Balmaseda, R.-H. Zhang, and Z.-Z. Hu, 2012b: Ensemble ENSO hindcasts initialized from multiple ocean analyses. *Geophys. Res. Lett.*, **39**, L09602, doi:10.1029/2012GL051503.

——, ——, M. A. Balmaseda, J. L. Kinter III, P. Peng, Z.-Z. Hu, and L. Marx, 2013a: Improved reliability of ENSO hindcasts with multi-ocean analyses ensemble initialization. *Climate Dyn.*, **41**, 2785–2795, doi:10.1007/s00382-013-1965-8.

——, G.-Q. Zhou, R.-H. Zhang, and Z. Sun, 2013b: Improving ENSO prediction in a hybrid coupled model with an embedded entrainment temperature parameterization. *Int. J. Climatol.*, **33**, 343–355, doi:10.1002/joc.3426.

——, B. Huang, R.-H. Zhang, Z.-Z. Hu, A. Kumar, M. A. Balmaseda, L. Marx, and J. L. Kinter III, 2014: Salinity anomaly as a trigger for ENSO events. *Sci. Rep.*, **4**, 6821, doi:10.1038/srep06821.

——, and Coauthors, 2015: ENSO prediction in Project Minerva: Sensitivity to atmospheric horizontal resolution and ensemble size. *J. Climate*, **28**, 2080–2095, doi:10.1175/JCLI-D-14-00302.1.